A&A, 702, A57 (2025)
https://doi.org/10.1051/0004-6361/202555816


Astronomy & Astrophysics

# RUBIES: A spectroscopic census of little red dots

## All point sources with v-shaped continua have broad lines

Raphael E. Hviding[1,⋆], Anna de Graaff[1], Tim B. Miller[2], David J. Setton[3,⋆⋆], Jenny E. Greene[3], Ivo Labbé[4], Gabriel Brammer[5,6], Rachel Bezanson[7], Leindert A. Boogaard[8], Nikko J. Cleri[9], Joel Leja[9], Michael V. Maseda[10], Ian McConachie[10], Jorryt Matthee[11], Rohan P. Naidu[12,⋆⋆⋆], Pascal A. Oesch[13,5,6], Bingjie Wang (王冰洁)[9], Katherine E. Whitaker[14,5], and Christina C. Williams[15]

[1] Max-Planck-Institut für Astronomie, Königstuhl 17, D-69117 Heidelberg, Germany
[2] Center for Interdisciplinary Exploration and Research in Astrophysics (CIERA), Northwestern University, 1800 Sherman Ave, Evanston, IL 60201, USA
[3] Department of Astrophysical Sciences, Princeton University, 4 Ivy Lane, Princeton, NJ 08544, USA
[4] Centre for Astrophysics and Supercomputing, Swinburne University of Technology, Melbourne, VIC 3122, Australia
[5] Cosmic Dawn Center (DAWN), Copenhagen, Denmark
[6] Niels Bohr Institute, University of Copenhagen, Jagtvej 128, Copenhagen, Denmark
[7] Department of Physics and Astronomy and PITT PACC, University of Pittsburgh, Pittsburgh, PA 15260, USA
[8] Leiden Observatory, Leiden University, PO Box 9513, NL-2300 RA Leiden, The Netherlands
[9] Department of Astronomy & Astrophysics; Institute for Computational & Data Sciences; Institute for Gravitation and the Cosmos; The Pennsylvania State University, University Park, PA 16802, USA
[10] Department of Astronomy, University of Wisconsin-Madison, Madison, WI 53706, USA
[11] Institute of Science and Technology Austria (ISTA), Am Campus 1, 3400 Klosterneuburg, Austria
[12] MIT Kavli Institute for Astrophysics and Space Research, 70 Vassar Street, Cambridge, MA 02139, USA
[13] Department of Astronomy, University of Geneva, Chemin Pegasi 51, 1290 Versoix, Switzerland
[14] Department of Astronomy, University of Massachusetts, Amherst, MA 01003, USA
[15] NSF National Optical-Infrared Astronomy Research Laboratory, 950 North Cherry Avenue, Tucson, AZ 85719, USA

Received 4 June 2025 / Accepted 29 July 2025

**ABSTRACT**

The physical nature of little red dots (LRDs), a population of compact red galaxies revealed by JWST, remains unclear. Photometric samples were constructed from varying selection criteria with limited spectroscopic follow-up available to test intrinsic spectral shapes and the prevalence of broad emission lines. We used the RUBIES survey, a large spectroscopic program with wide color-morphology coverage and homogeneous data quality, to systematically analyze the emission-line kinematics, spectral shapes, and morphologies of ∼1500 galaxies at $z > 3.1$. We identified broad Balmer lines via a novel fitting approach that simultaneously models NIRSpec/PRISM and G395M spectra, yielding 80 broad-line sources with 28 (35%) at $z > 6$. A large subpopulation naturally emerged from the broad Balmer line sources, with 36 exhibiting v-shaped UV-to-optical continua and a dominant point source component in the rest-optical; we define these as spectroscopic LRDs, constituting the largest such sample to date. Strikingly, the spectroscopic LRD population is largely recovered when either a broad line or rest-optical point source is required in combination with a v-shaped continuum, suggesting an inherent link between these three defining characteristics. We compared the spectroscopic LRD sample to published photometric searches. Although these selections have high accuracy, 80%−95% down to F444W < 26.5, only 50%−80% of the RUBIES LRDs were photometrically identified, depending on the selection criteria used. The remainder were missed due to a mixture of faint rest-UV photometry, comparatively blue rest-optical colors, or highly uncertain photometric redshifts. Our findings highlight that well-selected spectroscopic campaigns are essential for robust LRD identification, while photometric criteria require refinement to capture the full population.

**Key words.** galaxies: active – galaxies: high-redshift

## 1. Introduction

The James Webb Space Telescope (JWST; Gardner et al. 2023) has revealed a remarkable population of high-redshift sources with extremely red rest-optical colors. These sources span a broad redshift range ($z \sim 1-10$; de Graaff et al. 2025a) and show diverse morphological properties, ranging from unresolved point sources to large disks that extend out to several kiloparsecs (e.g. Baggen et al. 2023; Furtak et al. 2023; Pérez-González et al. 2023; Gibson et al. 2024; Williams et al. 2024; Xiao et al. 2025). Follow-up spectroscopy has revealed a variety of spectral properties. Although high equivalent width emission lines explain the red broadband colors of some sources (e.g., Larson et al. 2023), others indeed have red continua, which can be smoothly rising or show strong spectral breaks (e.g., Carnall et al. 2024; Cooper et al. 2025; Wang et al. 2024). Importantly, this diversity in properties also points to a mixture of physical interpretations,

⋆ Corresponding author: hviding@mpia.de
⋆⋆ Brinson Prize Fellow.
⋆⋆⋆ NHFP NASA Hubble Fellow.

including (dust-reddened) star formation, evolved stellar populations, or emission from active galactic nuclei (AGN).

A peculiar subset of red sources are distinguished by their highly compact nature, and are commonly referred to as little red dots (LRDs). While the term was originally coined by Matthee et al. (2024) to describe potential AGN with broad Balmer emission that appeared red and compact in JWST/NIRCam rest-optical imaging, its usage has since expanded. In particular, several independent searches aimed at identifying extremely massive galaxies within the first gigayear of the Universe relied on NIRCam photometry alone to select candidates based on very red observed rest-optical colors (F277W−F444W $\gtrsim$ 1), indicative of strong Balmer breaks, along with nondetections at wavelengths shorter than 1 μm, consistent with a Lyman-$\alpha$ break at $z \gtrsim 6$ (Labbé et al. 2023; Barro et al. 2024). These searches uncovered a population of objects with v-shaped continua: red in the rest-optical, but blue in the rest-UV, many of which also exhibit point-like morphologies in the long-wavelength (LW) NIRCam bands and have since also been referred to as LRDs.

Follow-up spectroscopy with JWST/NIRSpec of individual sources has suggested an intriguing link between compact, red photometric sources and broad-line AGN. The strongly lensed source with a v-shaped broadband spectral energy distribution (SED) of Furtak et al. (2023) was shown to have broad (FWHM $\sim 3000\,\mathrm{km\,s^{-1}}$) Balmer emission lines consistent with AGN emission (Furtak et al. 2024). Among the candidate massive galaxies at $z_{\rm phot} \sim 7$−9 identified by Labbé et al. (2023), one was spectroscopically confirmed as a broad-line AGN at $z_{\rm spec} = 5.6$ (Kocevski et al. 2023), while others were verified at high redshift and showed both strong Balmer breaks and broad Balmer lines (Wang et al. 2024). Greene et al. (2024) conducted the first systematic spectroscopic follow-up of photometric LRDs from Labbe et al. (2025) as part of the UNCOVER survey (Bezanson et al. 2024), finding that 9/12 sources (75%) exhibit broad Balmer emission. Collectively, these studies suggest a high incidence of broad-line AGN among some LRD samples, though the exact fraction appears sensitive to the selection criteria and highlights the need for uniform, large-scale spectroscopic follow-up.

If interpreted as AGN-dominated sources, the number density of LRDs would exceed that of the faint AGN expected from extrapolation of the quasar UV luminosity function by an order of magnitude (Matthee et al. 2024; Pizzati et al. 2025). Furthermore, if the LRDs were AGN with properties consistent with their lower-redshift counterparts, the implied high black hole masses would appear to greatly exceed local BH-galaxy scaling relations (e.g., Harikane et al. 2023; Maiolino et al. 2024; Furtak et al. 2024; Kokorev et al. 2023), though this may be, in part, due to biases in estimating host properties, AGN attenuation or bolometric luminosities, and/or black-hole masses (e.g., Li et al. 2025; Rusakov et al. 2025; Chen et al. 2025a). The population of LRDs may therefore have important implications for our understanding of the formation and growth history of supermassive black holes.

On the other hand, if the rest-optical continuum is dominated by starlight, it would imply the presence of very massive galaxies in the first gigayear (up to $10^{11}\,\mathrm{M_\odot}$ by $z \sim 7$−8; Labbé et al. 2023), requiring extremely efficient star formation that pushes the boundaries of the maximum stellar mass growth possible in the ΛCDM model (Boylan-Kolchin 2023). Combined with their highly compact morphologies, it would also imply that LRDs are the densest stellar systems in the Universe (Baggen et al. 2024; Guia et al. 2024; Ma et al. 2025; de Graaff et al. 2025b), exceeding observations and theoretical expectations of the maximum densities in star clusters (Hopkins et al. 2010; Grudić et al. 2019). However, this is unlikely to be true for all LRDs, as some show Balmer breaks that are far stronger than can be produced with evolved stars alone (de Graaff et al. 2025b; Naidu et al. 2025).

This uncertainty has motivated systematic searches aimed at quantifying the prevalence of LRDs and characterizing their population-wide properties, which so far have focused primarily on photometry (e.g., Labbe et al. 2025; Barro et al. 2024; Kokorev et al. 2024; Kocevski et al. 2025; Pérez-González et al. 2024; Akins et al. 2024). Although the precise selection criterion used differs for each study, all require a red rest-optical continuum, most require that the rest-optical morphology is unresolved or very compact, and some additionally require that the continuum is v-shaped, i.e., a blue rest-UV continuum as well as a red rest-optical continuum. Notably, the inferred number densities and SED properties vary greatly depending on the selection method and modeling choices. Whereas some favor an AGN-dominated interpretation of the SED, using the LRD population to quantify the AGN bolometric, luminosity and/or black hole mass functions (e.g., Labbe et al. 2025; Kocevski et al. 2025; Kokorev et al. 2024), others argue that the SEDs may be best described by stellar populations and that LRDs therefore represent a class of dust-obscured star-forming galaxies (Pérez-González et al. 2024) or dust-obscured post-starburst galaxies (e.g., Labbé et al. 2023; Labbe et al. 2024; Williams et al. 2024; Wang et al. 2024, 2025). Hainline et al. (2025) also point out that a large fraction of sources may not have red continua, but that the broadband colors may be boosted by strong emission lines. Finally, brown dwarfs can also appear to have v-shaped broadband photometric SEDs and are necessarily point sources (e.g., Langeroodi & Hjorth 2023; Greene et al. 2024; Hainline et al. 2024, 2025).

Although targeted spectroscopic follow-up of small LRD samples has revealed a high fraction of broad Balmer emission lines and v-shaped continua, it remains unclear how these findings extend to the broader photometric samples in the literature, whose selection criteria can vary significantly. For example, Pérez-González et al. (2024) compiled spectra from various spectroscopic surveys for 18 sources in their photometric LRD sample and found that only 3 show broad Balmer emission, three times fewer than reported in the systematic follow-up by Greene et al. (2024). These discrepancies have critical implications for the interpretation of the physical properties of LRDs.

To robustly link the spectral properties of LRDs to these large photometric samples therefore requires comprehensive follow-up spectroscopy of photometric candidates. The JWST/NIRCam grism has been demonstrated to be highly successful at determining robust redshifts and selecting broad Balmer emission lines (e.g., Matthee et al. 2024; Naidu et al. 2024; Sun et al. 2025; Lin et al. 2024, 2025), but simultaneous coverage of forbidden lines such as [O III] is still rare, making it difficult to rule out broadening from stellar feedback and outflows. Only JWST/NIRSpec can reveal the continuum shape and at the same time kinematically resolve multiple emission lines. However, such targeted follow-up often leads to a complex spectroscopic selection function, and robustly quantifying the fraction of photometrically selected LRDs with broad Balmer lines and v-shaped continua is therefore challenging.

The Red Unknowns: Bright Infrared Extragalactic Survey (RUBIES; de Graaff et al. 2025a) was designed to deliver a large spectroscopic dataset with a well-characterized selection function: RUBIES has observed a large number (∼300) of red sources

without morphological pre-selection, while at the same time has sampled several thousand galaxies with a broad distribution in color space. For this paper, we used the full RUBIES dataset at $z > 3.1$ to robustly quantify the prevalence of (1) broad Balmer emission lines, (2) v-shaped continua, and (3) a dominant point source in the rest-optical. As we show below, a population of spectroscopic LRDs, i.e., those that meet all three criteria, naturally arises from the data, hinting that these features may be physically interlinked.

In Section 2 we present an overview of the RUBIES survey and the relevant data used in this work. We describe our methodology for measuring typical LRD features in Section 3, while in Sect. 4 we explore the relationship between these characteristics to construct a spectroscopic LRD definition. Section 5 compares our results to existing photometric LRD selection techniques. Finally, we present our summary and discussion in Section 6. Where relevant, we assume a flat ΛCDM cosmological model with $\Omega_m = 0.3$ and $h = 0.7$. All magnitudes are reported using the AB system (Oke & Gunn 1983) and nondetections ($<1\sigma$) are reported as their $1\sigma$ upper limits.

## 2. Data and spectroscopic sample

The JWST Cycle 2 program RUBIES (GO-4233; PIs: de Graaff & Brammer) is a 60-hour spectroscopic survey with the NIRSpec microshutter array (MSA) that has observed ∼4500 high-redshift sources selected across ∼150 arcmin$^2$ from JWST Cycle 1 NIRCam imaging programs. A detailed description of the observing strategy, parent catalogs, and spectroscopic selection function, as well as the spectroscopic data reduction can be found in de Graaff et al. (2025a). In this section, we provide a brief summary of key details relevant to this work.

### 2.1. JWST imaging

The RUBIES targets were selected from two extragalactic deep fields, the Ultra Deep Survey (UDS) and Extended Growth Strip (EGS). Both fields have extensive photometric coverage from X-ray to radio wavelengths, and were central to the CANDELS and 3D-HST surveys (Grogin et al. 2011; Koekemoer et al. 2011; Brammer et al. 2012; Skelton et al. 2014). Public JWST/NIRCam imaging was obtained for these fields as part of multiple programs in Cycles 1−3.

For the EGS the majority of NIRCam imaging data comes from the Cosmic Evolution Early Release Science Survey (CEERS; GO-1345, PI: Finkelstein; Finkelstein et al. 2025). This imaging spans approximately 80 arcmin$^2$ (Bagley et al. 2023) in 7 different NIRCam filters (F115W, F150W, F200W, F277W, F356W, F410M, F444W), with a $5\sigma$ point source depth of 28.6 mag at 4 μm. In addition, the Cycle 1 program GO-2234 (PI: Bañados; Khusanova et al., in prep.) obtained NIRCam/F090W imaging over the same footprint as CEERS.

The UDS was one of two fields observed as part of the Public Release IMaging for Extragalactic Research Survey (PRIMER; GO-1837; PI: Dunlop). This survey used the same 8 filters as the programs in the EGS, reaching a comparable typical depth (see Donnan et al. 2024), but for a larger area of ∼220 arcmin$^2$. Combined, these surveys therefore provide a homogeneous dataset for spectroscopic follow-up.

All imaging data were reduced with the `grizli` pipeline (Brammer 2023a), the details of which are described in Valentino et al. (2023). The resulting image mosaics have a pixel scale of 0.04″ and are publicly available from the DAWN JWST Archive[1] (DJA). The RUBIES targets were selected using version 7.2 of the DJA image mosaics; for this paper we used version 7.2 for the UDS mosaics and version 7.4 for the EGS mosaics to perform morphological modeling.

The RUBIES photometric parent catalog was constructed primarily from the public catalogs on the DJA, with photometry measured in circular apertures of diameter 0.5″ and photometric redshift measurements from `eazy` (Brammer et al. 2008). This catalog was thoroughly visually inspected to remove artifacts and stars and supplemented with a small number of candidate high-redshift ($z > 6.5$) sources from the photometric catalogs of Weibel et al. (2024).

We caution that the photometry in this parent catalog does not account for the wavelength-dependent point spread function (PSF) of JWST. To measure consistent colors in this paper, we therefore cross-match our final spectroscopic sample, as described in Section 2.2, to the catalogs of Weibel et al. (2024), who provide photometry measured from image mosaics that were matched in resolution to the F444W filter using empirical PSF models. We use circular aperture flux measurements with diameter of 0.5″ to compute colors, and use the Kron flux measured in the F444W band as a measurement of the total flux.

### 2.2. RUBIES spectroscopy

The RUBIES dataset consists of 12 NIRSpec MSA pointings in the UDS and 6 pointings in the EGS, covering a total area of approximately 150 arcmin$^2$. The pointing locations were chosen to optimize the total number of high-priority targets across the survey. Priorities were assigned to sources in the parent catalog using a small number of parameters (see de Graaff et al. 2025a for full details): the total flux at 4 μm, F150W−F444W color, and photometric redshift. The highest priority red sources were selected by requiring F444W < 27 and F150W−F444W > 2 with no restriction on photometric redshift; high-priority high-redshift sources were selected by F444W < 27 and $z_{phot} > 6.5$ with visual vetting to remove low-redshift interlopers. The remainder of the catalog was rank-ordered using the source weight $W$, a quantity that is inversely proportional to the source number density in the parameter space of F444W, F150W−F444W and $z_{phot}$. In designing the masks, targets were assigned shutters in order of priority and weight.

In total there are 4444 unique spectroscopic targets. As the result of the prioritization strategy, this sample includes a large number of rare, red sources at $z > 1$ and the survey overall reaches high spectroscopic completeness (>70%) in sparsely populated regions in observed color space. Source morphology was explicitly not used in any of the target prioritization, and RUBIES therefore probes a large variation of red sources, ranging from LRDs to dust-obscured extended star-forming disks. At the same time, the survey includes a representative sample of the high-redshift population that is less red, providing a crucial census sample to place rare sources in context.

Of the 4444 targets, approximately 3000 were observed with both the low-resolution PRISM/CLEAR ($\mathcal{R} \sim 50-500$; 0.6−5.5 μm) and medium-resolution G395M/F290LP ($\mathcal{R} \sim 1000-1500$; 2.7−5.5 μm) disperser/filter combinations. The remainder were observed only with the G395M grating. Observations were taken by constructing 3-shutter slitlets for each target and performing a 3-point nodding pattern. The total exposure time is 48 min for each disperser.

[1] https://dawn-cph.github.io/dja/

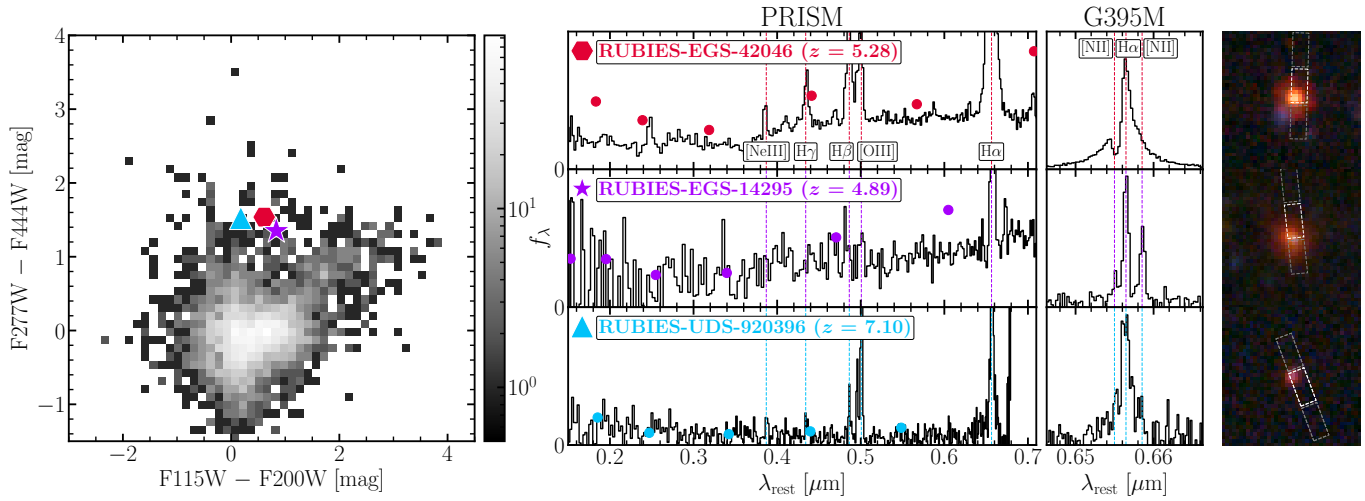


**Fig. 1.** Diversity of red high-redshift sources in RUBIES. Right: F115W−F200W vs. F277W−F444W for RUBIES sources with robust $z_{\rm spec} > 3.1$ (gray histogram), which populate a broad distribution in color space. Right: PRISM spectra and NIRCam photometry, G395M spectra (zoomed in on H$\alpha$), and $1'' \times 1''$ NIRCam F444W/F277W/F150W RGB images for three RUBIES targets that are close in color space. The top row shows a typical LRD, with a v-shaped continuum, broad H$\alpha$ emission line and very compact morphology. The middle row shows an extended red object with a v-shaped continuum, but narrow H$\alpha$ and [N II] emission. The red source in the bottom row is a point source with a relatively blue continuum, but appears as red due to high equivalent width emission lines, including a broad H$\alpha$ line. This demonstrates that sources with similar broadband photometric colors can have very different spectral properties.

The RUBIES spectra were reduced using version 3 of the `msaexp` pipeline (Brammer 2023b), as described in detail in Heintz et al. (2025) and de Graaff et al. (2025a). These reductions offer two types of background subtraction for the PRISM mode. To ensure that the spectral extractions of the PRISM and G395M spectra are matched, we use only the local background subtracted spectra in this paper, i.e., those obtained from the image differences between the three nodded exposures. Spectroscopic redshifts were measured with the `msaexp` template fitting and visually inspected to assign quality flags. Grading is fully described in Section 3.2 of de Graaff et al. (2025a); however, we note that a `grade` = 3 corresponds to a robust redshift. We note that RUBIES overall has a very high spectroscopic success rate, as approximately 90% (70%) of high-priority red sources (all sources) have robust redshifts. We find a total of 2014 sources with robust redshifts and both G395M and PRISM spectroscopy.

For a subset of sources ($N$ = 297), we also use the newly developed version 4 of `msaexp` (Brammer et al., in prep.). The most important change in version 4 is in the flux calibration, which was re-derived empirically from standard stars observed in a range of commissioning and calibration programs. Crucially, these new calibrations extend the nominal wavelength ranges of the PRISM and G395M dispersers by ±0.2 µm, enabling the measurement of [O III] and H$\alpha$ emission down to $z \sim 5.5$ and $z \sim 3.1$ in G395M compared to $z \sim 5.8$ and $z \sim 3.4$ respectively, and H$\alpha$ out to $z \sim 7.4$ in both dispersers compared to $z \sim 7.1$. We use these v4 reductions only for broad-line identification for sources at $z_{\rm spec} \in [3.1, 3.4]$ and $z_{\rm spec} > 6.9$, and rely on the v3 reductions for other analyses, i.e., continuum fitting.

Lastly, we add one serendipitous compact red source (F444W = 24.1) to our sample that was coincidentally observed as the neighbor of a lower-priority object (RUBIES-UDS-50432) in an outer slitlet. Using a custom spectral extraction using the global background, we determine that the source is at $z_{\rm spec}$ = 6.42 and could potentially be a bright LRD as preliminary visual inspections of its spectroscopy indicate a broad line and v-shaped continuum. This source is referred to as RUBIES-UDS-57040 going forward.

To select our final sample for uniform and robust broad line identification, we require a robust $z_{\rm spec}$, i.e., visually inspected `grade` = 3, and that either the H$\alpha$ or H$\beta$ line fall into the G395M defined as any pixels falling within 1000 km s$^{-1}$ of the emission line position predicted by the DJA $z_{\rm spec}$. This is especially relevant for robustly detecting broad lines at lower redshifts as the resolution of the PRISM disperser is very low ($\mathcal{R} < 100$) at <3 µm. In practice, this limits our sample to $z_{\rm spec} > 3.1$ with the extended coverage from the v4 reduction. This yields a sample of 1482 sources, with a median redshift of $z_{\rm spec}$ = 4.66 and maximum redshift of $z_{\rm spec}$ = 9.3, hereafter referred to as RUBIES sources with robust $z_{\rm spec} > 3.1$. Of these 1198 (80%) have PRISM spectroscopy; only these targets are used to to measure LRD features in the following sections. As shown in Figures 5 and 6 of de Graaff et al. (2025a), the $z \gtrsim 3$ sources in RUBIES have a broad distribution in color space, spanning not only a broad range in the color used for target prioritization, F150W−F444W, but also in F115W−F200W and F277W−F444W.

The diversity of our sample extends far beyond broadband colors. In Figure 1 we demonstrate that sources with similar observed colors can have drastically different spectral shapes, emission line properties, and emission line kinematics. In the top row, we present a prototypical LRD: a point-like red source with a v-shaped continuum and broad H$\alpha$ emission. The middle row shows a compact, yet resolved, dusty star-forming galaxy, which has a v-shaped continuum but narrow H$\alpha$ and [N II] emission. The bottom row shows an AGN, a point source with a relatively blue continuum that appears red in broadband photometry due to strong emission lines, including broad H$\alpha$ emission. Despite similar broadband colors, the sources span a wide range of morphologies, star formation histories, dust content, and ionizing mechanisms. The spectroscopic diversity of these sources underscores the importance of the RUBIES spectroscopic dataset for disentangling the nature of red JWST sources.

## 3. LRD features

In this section we aim to robustly measure photometric and spectroscopic features commonly associated with LRDs: a broad Balmer line in Section 3.1, a v-shaped continuum in Section 3.2, and a dominant rest-optical point source in Section 3.3.

### 3.1. Broad Balmer emission

Our goal is to robustly identify and measure broad emission components that are distinct from narrow line emission and uniquely associated with the Balmer lines, i.e., H$\alpha$ and H$\beta$. This requires differentiating broad Balmer emission from potential contamination by other broadening mechanisms, such as galactic outflows that might similarly affect forbidden lines, for example [O III].

#### 3.1.1. Simultaneous spectroscopic fitting

To impose the strictest constraints on the presence of broad emission lines, we introduce the `Python` package `unite`[2], Uniform NIRSpec Inference (Turbo) Engine (Hviding 2025), to simultaneously fit all available NIRSpec spectra for each individual source within a given mask. Because extractions within a mask are performed using a consistent aperture, background subtraction, and trace extraction, we assume that the intrinsic source spectrum is the same across exposures. Differences between spectra arise primarily from the dispersion characteristics of the gratings, which affect the spectral resolution and sampling, as well as from relative calibration uncertainties between dispersers. By jointly fitting these spectra, we leverage the complementary wavelength coverage, signal-to-noise (S/N), and resolution to enhance our sensitivity to broad emission features. For sources observed in multiple masks, we treat each mask independently, as differing apertures preclude the assumption of a shared underlying spectrum. The mask with the highest S/N spectra is taken as the fiducial mask for a source.

We begin by constructing a statistical model for emission lines and continua: we include the H$\alpha$ and H$\beta$ emission lines along with the [O III]$\lambda\lambda$4960, 5008 Å, [N II]$\lambda\lambda$6549, 6585 Å, and [S II]$\lambda\lambda$6718, 6732 Å doublets. Our fitting region is centered around each line and extends $\pm 15\,000\,\mathrm{km\,s^{-1}}$. Overlapping regions are merged, resulting in two primary fitting windows: 4619 Å–5258 Å and 6222 Å–7070 Å in the rest frame. Each region is modeled with a linear continuum, where the slope $\theta$ follows a noninformative prior, $\theta \sim \mathcal{U}(-\pi/2, \pi/2)$, and the height is drawn from a broad uniform prior based on an initial continuum estimate. Emission lines are modeled as Gaussians, with redshift $z \sim \mathcal{U}(z_{\rm spec} - 0.005, z_{\rm spec} + 0.005)$, FWHM $w_{\rm narrow} \sim \mathcal{U}(0, 750)$ $\mathrm{km\,s^{-1}}$, and flux constrained to be positive, drawn from a broad uniform prior based on an initial flux estimate.

Because the default pipeline does not account for covariance in error propagation, we rescale the error spectrum in each fitting region to account for systematic over- or underestimation of uncertainties. We mask $\pm 3500\,\mathrm{km\,s^{-1}}$ around each expected emission line to isolate the continuum. The remaining region is fit with a weighted least squares (WLS) linear model from which we compute the reduced chi-squared, $\chi^2_\nu$. Assuming that the continuum is well described by a linear model, the normalized residuals should have unit variance. To enforce this, we multiply the error spectrum by $\sqrt{\chi^2_\nu}$ in each region and for each disperser. This correction ensures that uncertainties in the final fit reflect the true variance in the continuum, improving the reliability of emission line constraints. Across all RUBIES spectra in this work, we find a typical correction factor of $\sim 1.1 \pm 0.2$.

We build two physical models: a narrow model, consisting only of narrow emission lines, and a broad model, which includes additional broad Balmer emission lines. In the narrow model, all emission lines share a common redshift and intrinsic velocity width. The broad model extends this by incorporating two additional Gaussians for H$\alpha$ and H$\beta$. To ensure reliable broad line detection, these additional lines are constrained to share the same redshift as the narrow lines. However, their FWHM is drawn from the prior $w_{\rm broad} \sim \mathcal{U}(w_{\rm narrow} + 100, 2500)\,\mathrm{km\,s^{-1}}$. For both models, the [O III] and [N II] flux ratios are fixed to the quantum-mechanically derived values of 1:2.98 and 1:2.95 respectively (Galavis et al. 1997).

Fitting the physical model to each spectrum requires accounting for several instrumental and observational effects. First, emission lines are broadened by the line-spread function (LSF), using the NIRSpec LSF curves of an idealized point source obtained with `msafit` (de Graaff et al. 2024). Because these are model LSFs rather than empirical calibrations, we introduce a scale factor drawn from a prior, $s_{\rm LSF} \sim \mathcal{N}(1.2, 0.1)$, truncated to [0.9, 1.5], to adjust for potential deviations. To address systematic flux offsets between the G395M and PRISM spectra observed in de Graaff et al. (2025a), we introduce a flux scale prior. The G395M scale is fixed at 1, while the PRISM scale follows $s_{\rm flux} \sim \mathcal{N}(1.1, 0.2)$, truncated to [0.5, 1.7], reflecting the observed range. Similarly, we account for pixel offsets between the two dispersers, with the G395M offset fixed at 0 and the PRISM offset drawn from $\delta_{\rm px} \sim \mathcal{U}(-0.3, 0.7)$ px. The choice of G395M as the reference is arbitrary and symmetric, ensuring that the relevant fluxes and redshifts remain recoverable for either disperser. Finally, to account for NIRSpec detector's undersampling of the LSF, the model is integrated in each pixel, rather than computed at the pixel center, before comparison with the observed data.

We implement these models using `NumPyro` (Phan et al. 2019), a probabilistic programming library built on top of `JAX` (Bradbury et al. 2018). Leveraging `JAX`'s automatic differentiation and Just-In-Time (JIT) compilation, `NumPyro` allows us to efficiently define and sample from our joint Bayesian model. We employ Markov chain Monte Carlo (MCMC) using the No-U-Turn Sampler (NUTS; Hoffman & Gelman 2014) with one chain comprised of 250 warmup steps and 500 posterior samples, ensuring robust convergence diagnostics and a typical runtime of <10 seconds for a typical source. Finally, to compare the relative model fits, we compute the Widely Applicable Information Criterion (WAIC) (Watanabe & Opper 2010), which accounts for model complexity while estimating out-of-sample predictive accuracy.

We present an example of our simultaneous broad and narrow fitting for RUBIES-EGS-926125 and RUBIES-EGS-966323 in Figure 2. The latter source was not conclusively identified as a broad-line source in Kocevski et al. (2025), denoted as CEERS-9083, or Wang et al. (2024). Due to the low S/N in the G395M spectrum and the relatively narrow width of the broad component, the broad-line was not identified from single spectrum fitting. By simultaneously leveraging the resolution of the G395M to constrain the narrow line width and the S/N of the PRISM to detect deviations from the derived width, the broad line is measured with a $\Delta$WAIC = 55, i.e., a $>6\sigma$ detection.

[2] `unite` is hosted on GitHub with a v1 release coming soon.

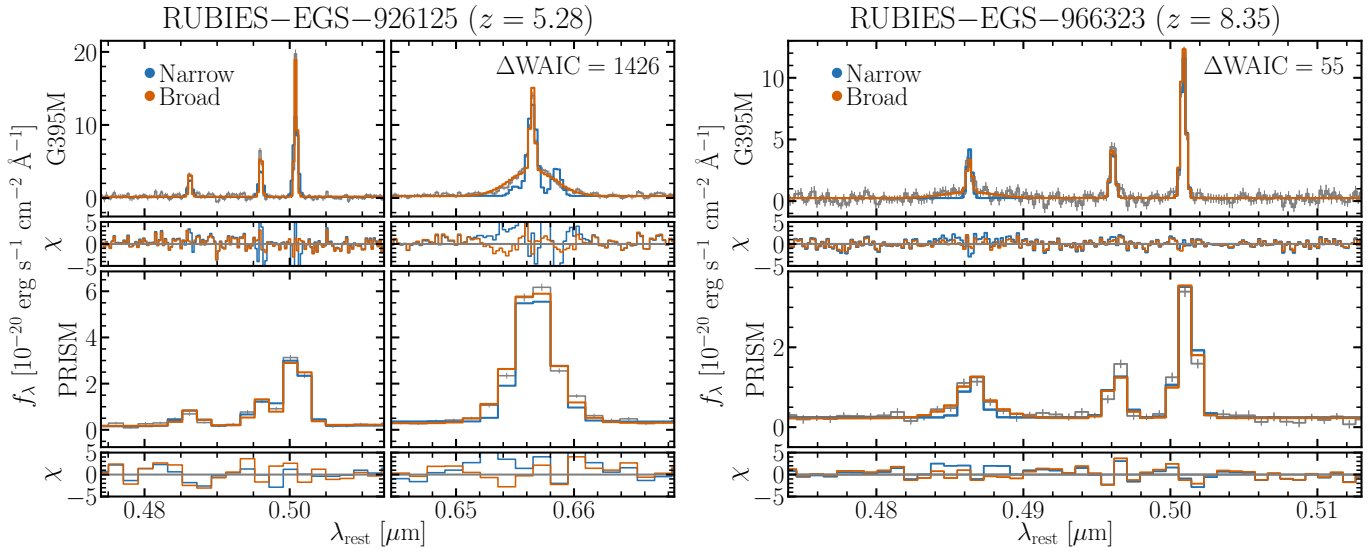


**Fig. 2.** Zoomed-in images of the spectroscopic fits for RUBIES-EGS-926125 (left) and RUBIES-EGS-966323 (right) using narrow (blue) and broad (orange) models for both G395M (top) and PRISM (bottom) spectra along with their residual deviations. We plot the maximum posterior sample from the MCMC fitting. Simultaneous fitting leverages all available data to constrain linewidths in both gratings across different wavelength regimes. For 926125 we show both the H$\beta$ + [O III] and H$\alpha$ + [N II] complexes, while for 966323 we only have coverage of the H$\beta$ + [O III] complex. We note that a broad component could not be conclusively fit in 966323 from the PRISM or G395M spectrum alone in Wang et al. (2024) or Kocevski et al. (2025), but is detected in this work at the >6.5$\sigma$ level.

### 3.1.2. Broad line validation

While a broad Balmer line will lead to a better fit with our fitting setup, data quality (DQ) issues can lead to a statistically improved fit even when the line profile is not well described by two kinematic components. An initial examination of the data reveal several failure modes for our `unite` fits: spectral trace overlaps, low S/N, or large offsets between the PRISM and G395M dispersers. To minimize contamination from false positives, we therefore implement the following quality cuts:

1. A $\Delta$WAIC $>$ 11.8, corresponding to a confidence level greater than 3$\sigma$ is required, i.e., ensuring that the improvement in fit provided by the broad model is statistically significant over the narrow model alone.
2. $w_{\rm broad} > 1000\,{\rm km\,s^{-1}}$ to exclude narrow-line contamination or ambiguous features.
3. In spectra with both H$\alpha$ and H$\beta$ coverage, the flux of the broad H$\alpha$ must exceed the flux of the H$\beta$ in order to eliminate unphysical fits.

Following our quality cuts, three individuals (REH, AdG, JEG) visually inspected all 121 broad-line candidates. The inspectors identified 19 sources (15.7%) with no clear evidence for a broad component (requiring 2/3 agreement), finding these cases showed flux contamination in the G395M due to other traces or DQ artifacts near the edge of the spectral range. We refer to these, and any other fitting failures due to DQ issues as indeterminate broad sources and present the common failure modes in Appendix B. In addition, we also denote objects without H$\alpha$ coverage and no broad Balmer detection as indeterminate broad sources.

However, a detected broad Balmer line does not guarantee that the line is not due to phenomena that can broaden other narrow lines, such as star-formation-driven outflows. We therefore use information from forbidden transitions, such as [O III], to investigate the origin of the broad line. For nearly every $z_{\rm spec} \gtrsim 5$ galaxy we recover [O III] in the G395M grating, provided the line does not fall into a chip gap or encounter other DQ issues. To distinguish between these scenarios, we further refine our sample of 102 detected broad Balmer lines based on the following criteria:

1. $w_{\rm broad} \geq 1500\,{\rm km\,s^{-1}}$: we attribute the broadening to arise from nonstellar feedback origins and therefore be tied directly to the Balmer line itself ($N = 69$). While it is not impossible for feedback and outflows to generate velocities in excess of this limit, the number of these outflows even in AGN-driven scenarios, drops sharply beyond $1000\,{\rm km\,s^{-1}}$ (Hao et al. 2005; Leung et al. 2019; Förster Schreiber et al. 2019). In addition, we note that we still visually inspect the forbidden-line properties where available for this sample and find no evidence for comparable broadening in these lines.
2. $w_{\rm broad} < 1500\,{\rm km\,s^{-1}}$: we then examine other strong nebular emission lines where available in the G395M grating, such as [N II] or [O III].
   (a) If no other narrow lines are detected, typically due to a lack of [N II] paired with redshifts where [O III] falls out of the G395M spectrum ($z \lesssim 5$), the Balmer line is not classified as broad and is also referred to as an indeterminate broad source ($N = 19$).
   (b) If another narrow line is detected and there is equal broadening present in that line and/or significant residuals in its fit, as determined by 2/3 agreement, we do not consider the source to be a broad Balmer line source ($N = 3$).
   (c) If another narrow line is detected and there is no broadening present, then the Balmer line is considered to be broad ($N = 11$).

We therefore conclude with a robust broad Balmer line sample of 80 galaxies and three with broadening in all narrow lines. The availability of both sensitive PRISM and higher-resolution G395M grating spectra allows for robust broad-line selection, yielding one of the largest sample of broad-line objects to date at $z > 4$ (Harikane et al. 2023; Maiolino et al. 2024; Kocevski et al. 2023; Taylor et al. 2025a; Juodžbalis et al. 2025; Lin et al. 2024, 2025; Zhuang et al. 2025). The broad Balmer line sample is

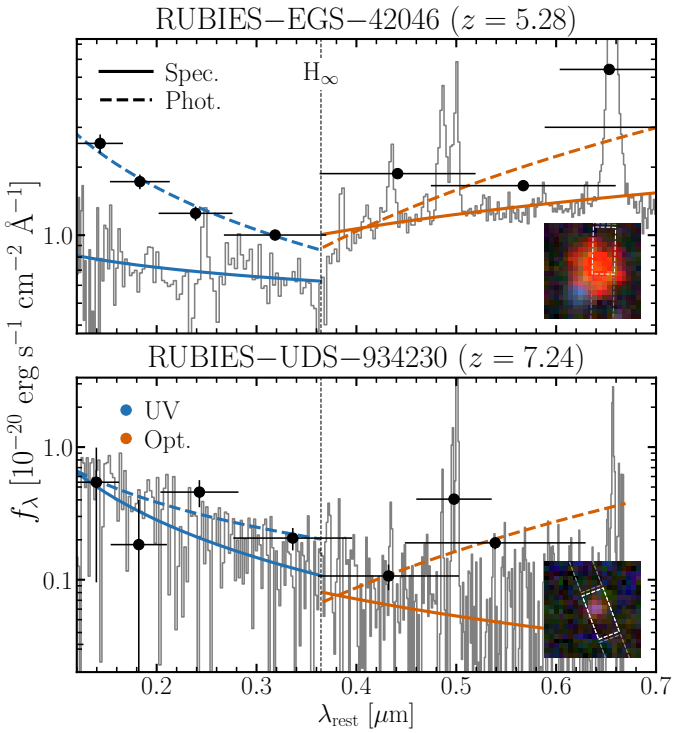


**Fig. 3.** Rest-UV (blue) and rest-optical (orange) continuum fitting of RUBIES-EGS-42046 (top) and RUBIES-UDS-934230 (bottom) from PRISM spectroscopy (solid) and NIRCam photometry (dashed). In the insets are the 0.5″×0.5″ NIRCam F444W/F277W/F150W RGB cutouts of the sources. We emphasize that spectroscopic rest-optical continuum fitting can mitigate the effect of strong emission lines, but can suffer in S/N in the rest-UV where the spectrum is fainter or cannot capture extended rest-UV emission due to slit losses. RUBIES-EGS-42046 is identified as a spectroscopic v-shape, while RUBIES-UDS-934230 is not despite a red photometric rest-optical color.

presented in Appendix B, including examples of failures of the fitting due to DQ issues.

Our emission line model, i.e., Gaussian profiles with uniform priors, is optimized for broad-line detection rather than detailed characterization. We caution that the reported FWHM values may not best represent the physical system, especially as LRDs often exhibit extended line wings that may be better modeled with Lorentzian functions (Wang et al. 2025; de Graaff et al. 2025b; Naidu et al. 2025; Rusakov et al. 2025; Labbe et al. 2024). Future work will address the full emission-line profile modeling taking these intricacies into account.

### 3.2. V-shaped continuum

To robustly measure the continuum shape of LRDs, we adapt and extend the fitting method described in Setton et al. (2024) to measure spectral slopes from both PRISM spectroscopy and NIRCam photometry. As established in Setton et al. (2024), the break in LRDs preferentially occurs at the Balmer limit of 3645 Å ($H_\infty$) in a sample selected independent of broad-line width. We therefore fix the continuum break location and fit the data on either side of the Balmer limit. For the rest-UV, we fit the range from 1200 Å–$H_\infty$, and for the rest-optical, we fit the range from $H_\infty$–7000 Å. The continua ranges are fit using a power law of the form $f_\lambda = a \cdot \lambda_{\rm rest}^{\beta}$ with nonlinear least squares optimization.

#### 3.2.1. Photometric continuum

We measure the continuum slopes from photometry by using all available wide NIRCam photometric bands whose central wavelength lie within the aforementioned spectral ranges. In addition, in order to fit a slope we require at least two photometric filters be available in the given spectral range. Since our primary goal in this section is to characterize the intrinsic continuum shape, we only measure photometric continua for sources with accompanying PRISM spectroscopy.

#### 3.2.2. Spectroscopic continuum

In order to mitigate the effect of strong emission lines, we mask the rest-frame spectrum ±50 Å around the H$\alpha$, H$\beta$, H$\gamma$, H$\delta$, He I$\lambda\lambda$4471, 6680 Å, [O II], and [Ne III] lines along with the [O III] and [N II] doublets. In addition, we require at least 25 wavelength elements be present after applying the emission line mask to fit a slope. While the photometric and spectroscopic continuum fits are performed independently, we use the photometry as evidence for blue rest-UV slopes as the rest-UV faintness or slit losses can lead to low continuum sensitivity. However, we always require a measurement of the rest-optical continuum from the spectroscopy. To define a source as v-shaped from spectroscopy, we impose the following criteria:

1. A blue rest-UV continuum with a nonnegative fit: $\beta_{\rm UV} < -0.2$ detected at the $2\sigma$ level and $a_{\rm UV} > 0$ from either spectroscopy or photometry.
2. A red rest-optical continuum with a nonnegative fit: $\beta_{\rm opt}$ (Spec.) $> 0$ detected at the $2\sigma$ level and $a_{\rm opt}$ (Spec.) $> 0$.
3. $\beta_{\rm opt}-\beta_{\rm UV} > 0.5$ using the rest-UV slope from spectroscopy if it satisfies our blue rest-UV continuum cut in spectroscopy, otherwise from photometry.

We are able to measure spectroscopic continua in 1158 (97%) of our robust $z_{\rm spec} > 3.1$ sample with PRISM spectroscopy; of these 55 (5%) are classified as v-shaped.

In Figure 3, we present the continuum fits for RUBIES-EGS-49140 and RUBIES-UDS-934230 using both photometric and spectroscopic data. Although both methods fit the data well, they differ in their results. While the photometry is often able to provide a higher S/N measurement, particularly in the rest-UV, it is significantly impacted by emission line contamination in broadband photometry, leading to different inferred red-optical slopes. However, photometry also can find bluer rest-UV slopes due to the extended UV 'fluff' often seen in LRDs (Labbe et al. 2024; Rinaldi et al. 2024; Chen et al. 2025b), which can be lost in spectroscopy due to slit losses.

### 3.3. Rest-optical point source morphology

Our morphological analysis addresses two key questions: (1) Is the source spatially resolved? and (2) if resolved, is there still a dominant point source component? We first assess basic resolvability in Section 3.3.1, recognizing that Sérsic profile fitting inherently assumes extended emission and requires careful calibration against known point sources. In addition, Section 3.3.2 will investigate whether resolved sources still contain a dominant nuclear point source component.

We characterize unresolved sources by performing Sérsic profile fits using `pysersic` (Pasha & Miller 2023) on all LW NIRCam bands, employing empirical PSFs from Weibel et al. (2024) for convolution. Our analysis requires S/N > 10 per filter and adopts uniform priors for the Sérsic index, $n \sim \mathcal{U}(0.65, 6)$,

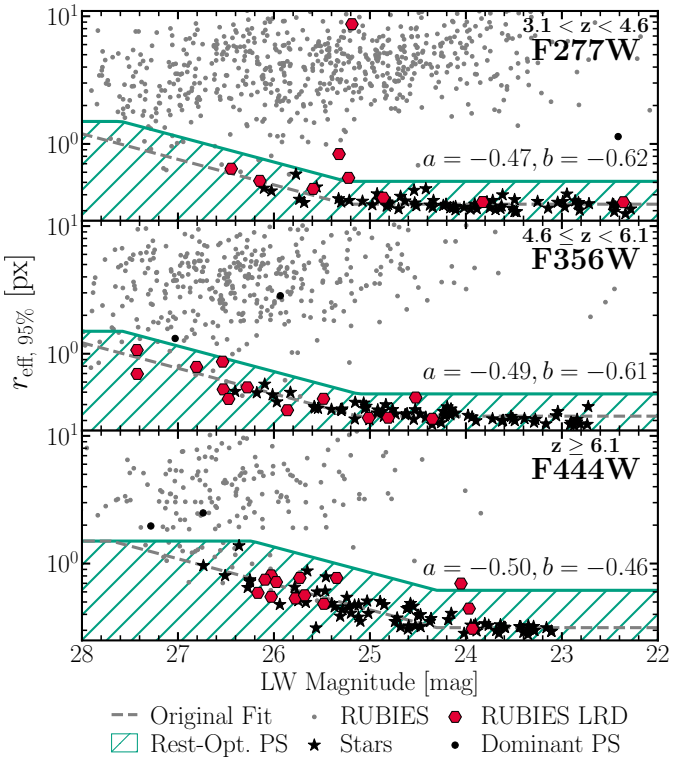


**Fig. 4.** Stellar locus and morphological classification in LW NIRCam filters. The black stars show the 95th percentile effective radius posterior ($r_{\rm eff,95\%}$) vs. magnitude for reference stars, with the best-fit stellar locus (gray dashed line). We classify galaxies as point sources (green hashed area) if they fall below the $+4\sigma_{\rm resid}$ offset of this relation ($r_{\rm rsv}$; green line). The gray circles show all RUBIES sources with robust $z_{\rm spec} > 3.1$, red hexagons highlight spectroscopic LRDs (Section 4.2), and black circles mark non-LRD sources with dominant point-sources (Section 3.3.1), plotted in the LW filter that traces the rest-5500 Å flux.

and effective radius, $r_{\rm eff} \sim \mathcal{U}(0.25, 25)$ px. The posterior distributions for the morphological parameters are sampled using the NUTS sampler implemented in `NumPyro` using 2 chains with 1000 warm up and 1000 sampling steps each. We validate fits by requiring $\hat{r} < 1.05$, minimum effective sample size of 250 across all parameters, and $\chi^2/(\#\,\mathrm{px}) < 2$ to rule out poor sampling or large residuals.

### 3.3.1. Rest-optical unresolved morphology

We first begin by assessing if the source is spatially resolved at all, i.e., can we robustly detect spatially extended emission beyond the PSF? However, this is not straightforward from Sérsic profile fitting, which by definition assumes an extended profile. Even when a source's inferred radius approaches the lower bound of the prior, this reflects an imposed modeling choice. While the prior limit can be adjusted, the interpretation ultimately depends on the precision of the PSF model, and there is no definite threshold for declaring a source resolved. We therefore perform Sérsic profiles to our robust $z_{\rm spec} > 3.1$ sample and a sample of stars which are known point sources and thus unresolved.

We begin by selecting a sample of stars in the UDS field starting with the same criteria used in Weibel et al. (2024) but extending down to fainter magnitudes, $23 < m_{\rm F444W} < 27$, to better match the brightness of sources discussed in this study. To eliminate contaminants from this selection, typically compact galaxies at $1 < z < 4$, we require that stars satisfy two additional color cuts: F200W−F444W < 0.75 and F150W−F200W < 0.1. Visual inspection of the images and SEDs confirms that these cuts yield a clean sample of stars. We ultimately identify 97 stars, to which we apply the same morphological fitting procedure and S/N cuts as used for our galaxy sample.

The posterior distributions of $r_{\rm eff}$ for the stellar sample are all bounded by the lower limit of the prior, with peaks in the distribution near 0.25 px and an extended tail out to larger radii. To quantify the spread of these posteriors, we plot the stellar magnitude against the 95th percentile of the $r_{\rm eff}$ posterior, $r_{\rm eff,95\%}$, for each LW NIRCam filter in Figure 4. For bright stars, we observe a floor in $r_{\rm eff,95\%}$ around 1/3 px, which we interpret as a systematic limit set by the PSF width and the accuracy of our PSF model. At magnitudes fainter than 25, $r_{\rm eff,95\%}$ increases, likely due to lower signal-to-noise ratios broadening the morphological posteriors. We observe that the slope of this increase is approximately 0.2 mag per $\log(r/\mathrm{px})$, consistent with a $\sqrt{\mathrm{flux}}$ dependence, confirming our expectation that the trend is driven by Poisson-dominated noise in the source centers.

We use the behavior of stellar magnitude versus $r_{\rm eff,95\%}$ to determine whether sources in our sample are spatially resolved. If a source falls within the locus defined by the stars, we classify it as unresolved. To assess this quantitatively, we fit a parametric model to the stellar distribution, described by a power-law with a plateau:

$$\log_{10}\left(\frac{r_{\rm rsv}}{\mathrm{px}}\right) = \max\left(0.2 \cdot (\mathrm{mag} - 24.5) + b,\ a\right)$$

where $a$ and $b$ are the parameters which are optimized separately for each filter. To ensure the curve fully encloses the stellar population, we compute the standard deviation of the residuals from the initial fit, shift both parameters upward by $+4\sigma_{\rm resid}$, and impose an upper limit of 1.5 px., resulting in curve we denote as $r_{\rm rsv}(m)$. The resulting curve, along with the best-fit $a$ and $b$ values for each filter, is shown in Figure 4.

This analysis reveals the tradeoff in point-source selection: our conservative morphological cut, i.e., imposing a strict 1.5 px upper limit, prioritizes sample accuracy at the potential cost of completeness. While effectively minimizing contamination from compact galaxies, this approach may exclude genuine point sources below ∼26 mag in F444W and ∼27.5 mag in F277W/F356W, where the stellar locus continues to rise beyond our size cutoff (Figure 4). We discuss the impact of this accuracy-completeness tradeoff on point-source selection in Section 5.2.

For each source in our sample we select the LW filter based on the redshift to ensure that the filter probes the rest-optical continuum around ∼5500 Å, i.e., F277W at $3.1 < z_{\rm spec} < 4.6$, F356W at $4.6 \leq z_{\rm spec} < 6.1$, and F444W at $z_{\rm spec} \geq 6.1$. A galaxy of magnitude $m$ in the relevant filter is then classified as unresolved if $r_{\rm eff,95\%} < r_{\rm rsv}(m)$. After removing bad fits and objects which are too faint in the given LW band to confidently measure, we are able to classify the morphologies for 1305 (88%) of our robust $z_{\rm spec} > 3.1$ sample; of these 1199 (92%) are identified as resolved, while the remaining 106 (8%) are considered unresolved.

### 3.3.2. Dominant point source component

For sources classified as resolved in Section 3.3.1, we investigate whether they still contain a dominant point-source component in their rest-optical emission. This analysis is

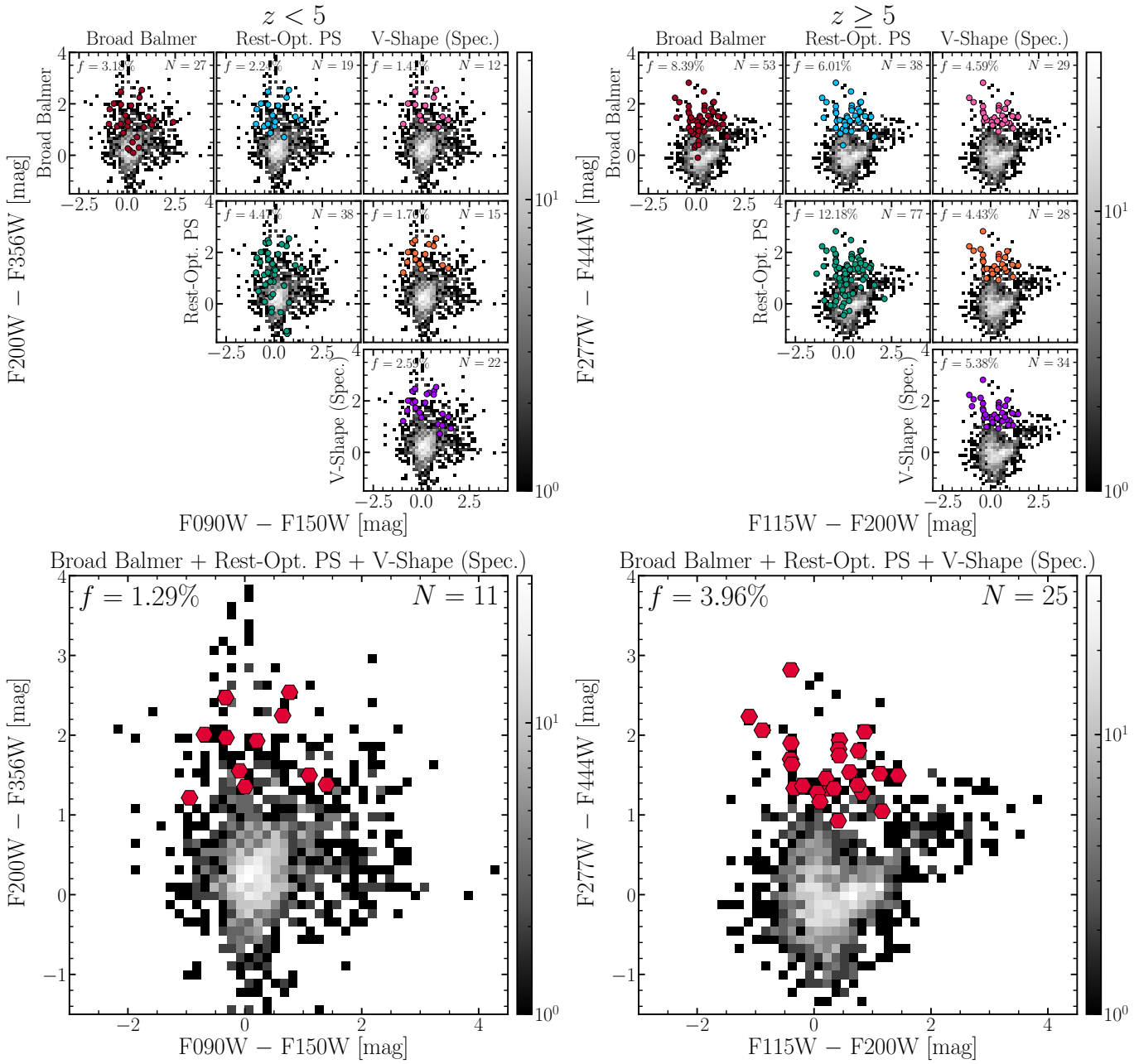


**Fig. 5.** Color-color space distribution of RUBIES sources with robust $z_{\rm spec} > 3.1$ (gray histogram). We divide the sample into $z_{\rm spec} < 5$ (right) and $z_{\rm spec} > 5$ (left) and show the NIRCam F090W−F150W vs. F200W−F356W and F115W−F200W vs. F277W−F444W, respectively, which approximately probe rest-UV vs. rest-optical colors. In the top row we plot objects that satisfy our condition for broad-line, unresolved, and v-shaped features, along with their combinations, above the full distributions of the parent sample in each redshift regime. In the bottom row we plot the objects that satisfy all three criteria. Each panel includes the total number of objects shown and the fraction of the represented sample. The points are colored as in Figure 7.

particularly relevant for understanding systems where an unresolved nucleus might coexist with extended host emission. However, decomposing these components is inherently challenging due to model dependencies and prior choices. We therefore restrict this analysis to sources that already show either broad Balmer lines or v-shaped continua ($N = 32$).

We perform two-component modeling using `pysersic`, fitting each source with a combination of a point source and a Sérsic profile. This largely follows the same procedure for the Sérsic profile fitting above, but we tie the central positions of the two components and add an additional parameter $f_{\rm ps}$, the fraction of flux in the point source component, with a uniform prior; $\mathcal{U}(0, 1)$. We classify a source as having a dominant point source if the 95th percentile of the point-source flux fraction exceeds 50% in the relevant LW filter. We find nine resolved objects with a dominant rest-optical point source: RUBIES-EGS-15825, RUBIES-UDS-23438, RUBIES-UDS-24447, RUBIES-EGS-28812, RUBIES-UDS-33938, RUBIES-EGS-46724, RUBIES-UDS-57040, RUBIES-UDS-167741, and RUBIES-UDS-840721. All nine show broad lines, perhaps unsurprisingly, as a broad Balmer line is a strong indicator of a bright central component. Of these five are also v-shaped.

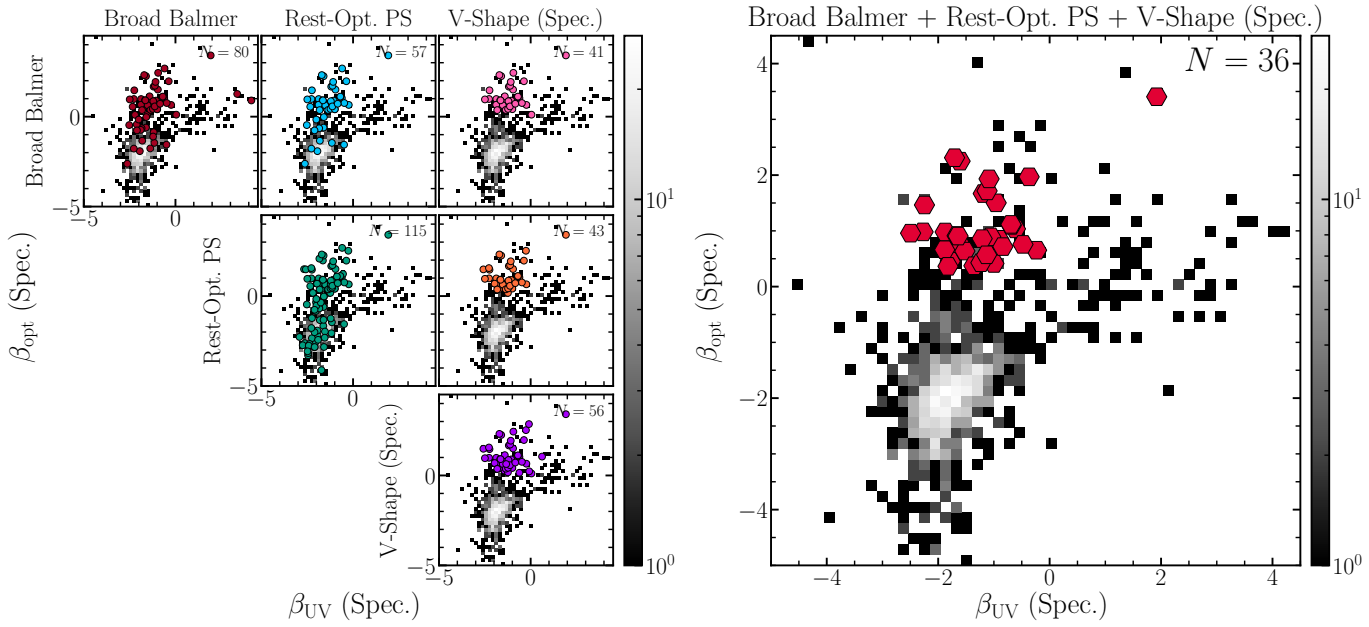


**Fig. 6.** $\beta_{\rm UV}$–$\beta_{\rm opt}$ space distribution of RUBIES sources with robust $z_{\rm spec} > 3.1$ (gray histogram). On the right, we plot objects that satisfy our condition for broad-line, unresolved, and v-shaped features, along with their combinations, above the full distributions of the parent sample. On the left, we plot the objects that satisfy all three criteria. The slopes are derived from PRISM spectroscopy and each panel includes the total number of objects plotted and their fraction of the represented sample. The points are colored as in Figure 7.

## 4. Spectroscopic LRD selection

Following Section 3, we are able to make a confident measurement for all three key characteristics of LRDs in 1019 RUBIES galaxies, i.e., the majority (69%) of our robust $z_{\rm spec} > 3.1$ sample (85% for the sample with PRISM spectroscopy). We can therefore robustly assess, for the first time, how the combination of a v-shaped continuum, a dominant point-source in the rest-optical, and a broad-line detection correlate among the high-redshift galaxy population.

### 4.1. Colors and intrinsic spectral slopes

In Figure 5 we plot the color-color distribution of our $z_{\rm spec} > 3.1$ sample and those that satisfy our condition for broad-line, unresolved, and v-shaped features. We divide the sample into two redshift bins, $z < 5$ and $z \geq 5$, and show NIRCam broadband colors that approximately probe rest-UV versus rest-optical colors in these regimes (F090W−F150W vs. F200W−F356W and F115W−F200W vs. F277W−F444W, respectively). We note that the difference in sample size between the two redshift bins is, in part, driven by the fact that the [O III] doublet is observed in the G395M grating for $z > 5$, which enables broad line identification down to smaller widths. However, broadband colors can be significantly impacted by emission line contamination, which depends on the spectroscopic redshift and the exact position of the emission line. We therefore show the corresponding intrinsic spectral slopes ($\beta_{\rm UV}$ vs. $\beta_{\rm opt}$) as derived from spectroscopy in Figure 6 to compare and contrast the distributions.

#### 4.1.1. Broad Balmer lines

We begin by investigating the observed colors and intrinsic slopes of the full sample with robustly detected broad Balmer emission. Broad-line sources tend to be redder in the rest-optical than the full spectroscopic sample, partly due to luminous broad H$\alpha$ emission, which can bias rest-optical colors by up to 0.8 mag. In contrast, when comparing to spectral slopes, we find that the broad-line sample spans wider range of rest-optical slopes. Their rest-UV slopes avoid the very reddest rest-UV tail, a region dominated by dusty star-forming galaxies.

#### 4.1.2. Rest-optical point sources

Galaxies that are unresolved or dominated by a point source at rest-optical wavelengths are distributed across much of color space. Again we see a preference for redder rest-optical colors compared to the full sample, although this may be in part due to the S/N criterion used to measure morphologies, i.e., that the rest-optical flux S/N > 10 (see Section 3.3). Similarly, when investigating spectral slopes, unresolved galaxies span the entirety of spectral-slope space populated by the sample, except for the reddest rest-UV slopes where the population is dominated by dusty star-forming galaxies that are typically larger in size.

#### 4.1.3. Spectroscopic v-shaped continuum

Enforcing a spectroscopic v-shaped selection will, by definition, restrict the sample to a limited area of spectral slope space. Similarly, v-shaped objects occupy a limited region of color space, but with slightly more scatter, attributable to emission line boosting, a moving break location that depends on the true source redshift, and low S/N in the bluest filters for the reddest sources. Roughly four-fifths of the v-shaped sources are unresolved. The remaining fifth may be related to the population of dusty starbursts with v-shaped continua and ALMA 1.2 mm detections from Labbe et al. (2025). Many of these galaxies in our sample, while resolved, are compact and show hallmarks of star formation, including strong but narrow H$\alpha$ and [N II], and may be related to other populations of compact, red, dusty, star-forming galaxies studied with JWST (e.g., Akins et al. 2023;

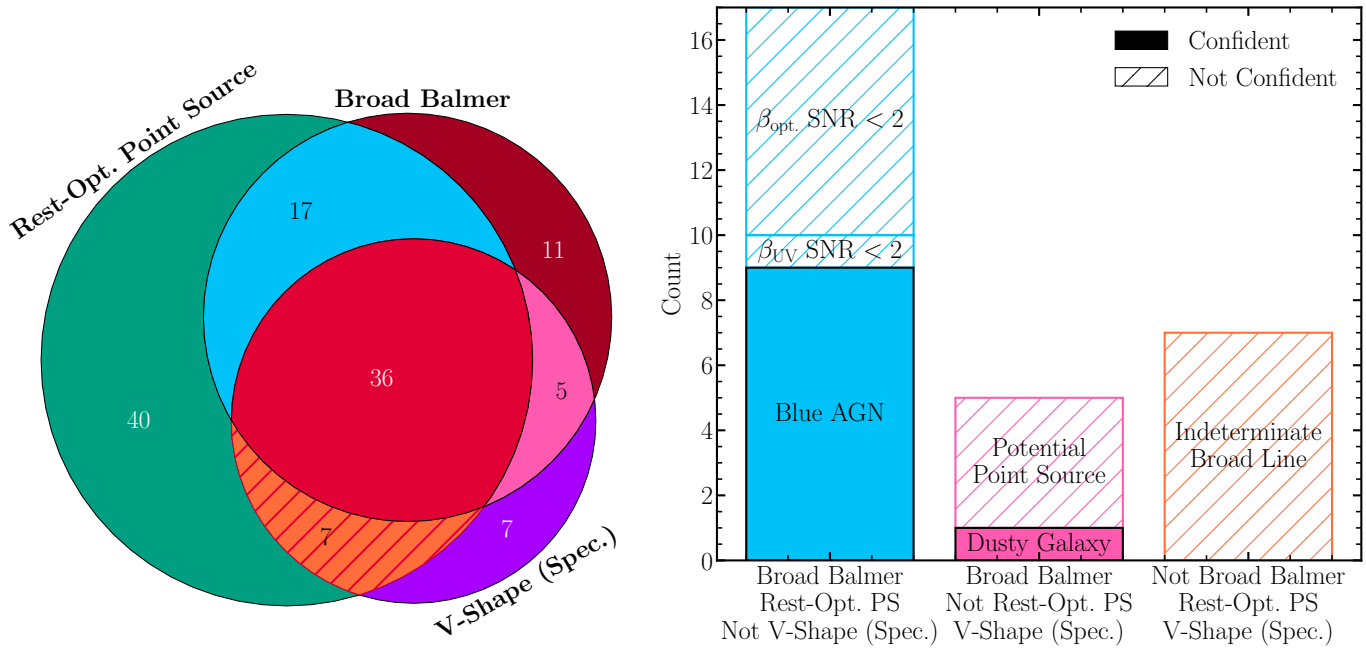


**Fig. 7.** Left: Euler diagram displaying the overlap between the three LRD characteristic criteria: a broad Balmer line, a dominant point source component at rest-optical wavelengths, and a spectroscopic v-shaped continuum. Right: Histogram showing the composition of overlaps in the Euler diagram where only two of the three features are measured. We note that objects with a rest-optical point source and a v-shaped continuum are 80% likely to have a broad line. In fact, in the remaining 20% we cannot reject a broad line, but our quality cuts restrict us from being fully confident. This suggests an underpinning physical link between the three LRD features.

Williams et al. 2024; Pérez-González et al. 2024; Barro et al. 2024).

### 4.2. Relationship between typical LRD features

We investigate how the full sample of galaxies with broad Balmer lines maps onto the v-shape and morphology selections. We find that the broad-line population divides into roughly three groups:

1. Resolved systems with broad lines. These span a variety of intrinsic slopes and likely represent galaxies with a nondominant AGN.
2. Unresolved systems with broad lines having blue rest-optical and rest-UV slopes that are likely comprised of typical AGN-dominated systems.
3. Broad-line systems with v-shaped continua that are spatially unresolved.

Figure 7 presents the Euler diagram exploring the relationship between all three features. Most remarkably, we find that if one starts with all sources having a v-shaped continuum, then either an unresolved rest-optical morphology or a broad-line selection will yield predominantly objects where all three features are robustly detected (>80%; red intersection). The remaining ~20% that do not satisfy the third criterion are overwhelmingly candidate LRDs rather than interlopers from distinctly different populations.

Specifically, while seven of the v-shaped rest-optical point sources (i.e., the orange intersection) technically lack a broad line detection, they are all classified as indeterminate broad lines, i.e., all are cases with data limitations where the presence of a broad line is ambiguous due to a DQ issue or a lack of coverage of the forbidden lines. Similarly, of the v-shaped with broad-line sources (pink intersection), we find they are all well-described by an additional point-source component, but that the prominence of this component falls below the strict limit (>50%) we require in this work. We note that one out of five sources, RUBIES-UDS-5496, shows strong [N II] emission not seen in any of our spectroscopic LRDs, as defined in Section 4.2. We assert that this is likely a dusty, star-forming galaxy hosting an AGN and not consistent with the population of spectroscopic LRDs explored in this work.

### 4.3. A spectroscopic definition of LRDs

We find that all intrinsically v-shaped spectra with dominant point sources in rest-optical imaging exhibit broad Balmer lines, provided the data quality permits their identification. This conclusion arises from a systematic analysis across galaxy color, morphology, and spectral shape, made possible by the RUBIES selection. Moving forward, we define a spectroscopic LRD as a source that simultaneously satisfies these three criteria: a broad Balmer line, a v-shaped continuum, and a dominant point source component in rest-optical imaging. Applying these criteria, we identify 36 spectroscopic LRDs in the RUBIES dataset, the largest such spectroscopic sample to date. NIRCam imaging, PRISM and G395M spectra, and broad line fits for these sources are provided in Appendix A. In addition, we identify seven v-shaped, rest-optical point sources for which broad lines could not be definitively confirmed. Although we consider it plausible that these sources are also spectroscopic LRDs, we do not include them in our spectroscopic LRD sample as DQ issues prevent the definitive measure of a broad Balmer line. These objects are nonetheless presented in Appendix A for completeness.

We briefly investigate how the properties of spectroscopic LRDs compare to the broad Balmer line sources and the robust $z_{\rm spec} > 3.1$ RUBIES sample. The left panel of Figure 8 demonstrates a wide redshift distribution for the broad-line objects, with the LRDs spanning a similar range in both redshift and

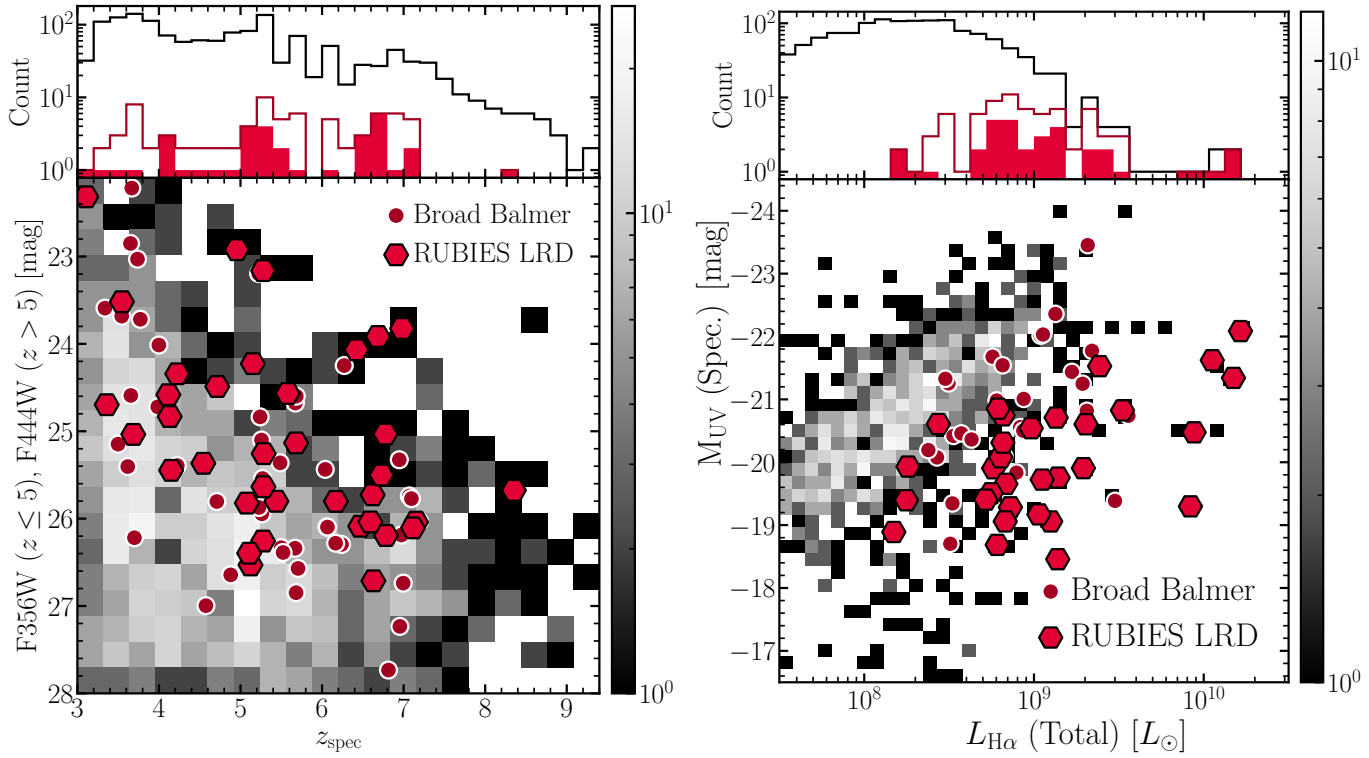


**Fig. 8.** Left: Redshift vs. NIRCam F356W (for $z_{\rm spec} \leq 5$) or F444W (for $z_{\rm spec} > 5$). Right: Absolute UV magnitude ($M_{\rm UV}$) at 1500 Å, derived from rest-UV spectroscopic slopes, is plotted against total, narrow plus broad, H$\alpha$ luminosity. RUBIES sources with robust $z_{\rm spec} > 3.1$ are shown as a gray histogram. Broad-line sources are indicated with dark red circles, and LRDs, defined as galaxies with v-shaped continua, broad Balmer lines, and dominant rest-optical point sources, are shown as light red hexagons. At fixed $L_{\rm H\alpha}$, LRDs are faint in the rest-UV compared to the full population. Conversely, extreme H$\alpha$ emitters ($L_{\rm H\alpha} \gtrsim 10^{10}\,{\rm M}_\odot$) are dominated by LRDs, i.e., LRDs constitute the most luminous H$\alpha$ emitters at fixed UV luminosity.

rest-optical magnitude. However, it is clear that LRDs are comprised of a distinct family of properties. Typical AGN, with broad lines and blue power-law continua, separate themselves primarily in continuum shape from the LRDs recovered in this work.

To further highlight their discrepancies, we compute UV luminosities at 1500 Å using the rest-UV continuum fits to the spectra from Section 3.2. In the right panel of Figure 8 we show the total, narrow plus broad, H$\alpha$ luminosity versus $M_{\rm UV}$ for the full robust $z_{\rm spec} > 3.1$ sample, the broad Balmer line sources, and the LRD sample. Although both the broad Balmer line sources and LRDs are offset from the bulk of the population, LRDs are the most H$\alpha$ luminous sources at all $M_{\rm UV}$. However, the LRDs also show a wide diversity of UV-to-optical ratios, exceeding the much narrower range in $L_{\rm H\alpha}$ at fixed $M_{\rm UV}$ spanned by the typical broad-line sources. We defer a full exploration of the interconnectedness of LRD properties and a physical interpretation to future work.

Overall, we conclude that LRDs – when selected using spectroscopy – comprise a distinct family of properties. Standard broad Balmer sources with power-law continua are well-represented in our sample, but are distinct in both continuum shape and H$\alpha$/UV luminosity from the spectroscopic LRDs.

## 5. Photometric LRD selection

Using an empirical approach to the RUBIES spectroscopic dataset, we have identified a population of LRDs that have broad Balmer emission lines, v-shaped continua, and compact rest-optical morphologies. This is in contrast to typical LRD searches that, to date, have often been based on photometry alone (e.g., Barro et al. 2024; Labbe et al. 2025; Kocevski et al. 2025; Kokorev et al. 2024; Akins et al. 2024). This raises the major question of whether photometric selection of LRDs yields the same sources as our spectroscopic selection. Greene et al. (2024) showed that ≈80% of photometric LRDs from the selection of Labbe et al. (2025) indeed have broad lines and v-shaped continua, albeit from a small sample of 12 sources.

In this section, we use our large spectroscopic sample of LRDs to evaluate the accuracy and completeness rates of popular photometric LRD selection strategies. We then investigate both contaminants and missed LRDs in the photometric samples.

### 5.1. Broad-line and LRD success rates

Two primary methods have been used to select LRD candidates in photometric surveys. The first is based on identification of v-shaped broadband photometric SEDs, and the second on the selection of red broadband rest-optical colors, sometimes additionally requiring blue rest-UV colors. All methods impose an additional compactness criterion. These different approaches have also been applied in the RUBIES parent fields, EGS and UDS, by three major photometric studies: Kocevski et al. (2025), which used a V-shape selection, and Kokorev et al. (2024) and Barro et al. (2024), which both employed multi-color selection; this provides an ideal opportunity to assess the effectiveness of each method. To quantify the success rates of these photometric methods we cross-match our

**Table 1.** Photometric LRD selection comparison.

| Photometric Constraint<br>Morphological Constraint | Kocevski et al. (2025)<br>Photometric V-Shape<br>Compact | Kokorev et al. (2024)<br>Multi-Color<br>Compact | Barro et al. (2024)<br>Multi-Color<br>Compact | F277W−F444W > 1.5<br>Single-Color<br>Rest-Opt. PS |
|---|---|---|---|---|
| RUBIES matches | 53/341 (15.54%) | 40[a]/259 (15.44%) | 101/440 (23.30%) | 31 |
| $z_{spec} > 3.1$ (& PRISM) | 47 (45) | 32 (28) | 84 (72) | 23 (22) |
| Brown dwarfs | 0 | 1 | 1 | 0 |
| Broad Balmer statistics ($z_{spec} > 3.1$) | | | | |
| Confident broad Balmer | 31/47 (65.96%) | 26/32 (81.25%) | 51/84 (60.71%) | 18/23 (78.26%) |
| Unknown (F444W > 26.5) | 10/47 (21.28%) | 1/32 (3.12%) | 15/84 (17.86%) | 3/23 (13.04%) |
| Unknown (F444W < 26.5) | 5/47 (10.64%)[b] | 5/32 (15.62%)[b] | 16/84 (19.05%)[c] | 2/23 (8.70%)[b] |
| Photometric sample makeup ($z_{spec} > 3.1$ & PRISM & F444W < 26.5) | | | | |
| *N* | 33 | 27 | 59 | 20 |
| Uncertain | 11/33 (33.33%) | 8/27 (29.63%) | 22/57 (38.60%) | 6/20 (30.00%) |
| Confident contamination | 1/33 (3.03%) | 2/27 (7.41%) | 7/57 (12.28%) | 1/20 (5.00%) |
| Spec. LRD | 21/33 (63.64%) | 17/27 (62.96%) | 28/57 (49.12%) | 13/20 (65.00%) |
| Spec. LRD accuracy | 21/22 (95.45%) | 17/19 (89.47%) | 28/35 (80.00%) | 13/14 (92.86%) |
| Spec. LRD completeness | 21/34 (61.76%) | 17/34 (50.00%) | 28/34 (82.35%) | 13/34 (38.24%) |

**Notes.** [a]Although there are 41 matches to Kokorev et al. (2024), we find that IDs 1470 and 59971 are the same object in that catalog. This object is only counted once in our analysis. [b]All uncertain broad Balmer lines with F444W < 26.5 are indeterminate broad, i.e., they lack [O III] or H$\alpha$ in G395M, or suffer from a DQ issue. [c]For Barro et al. (2024), 12/16 (75%) uncertain broad Balmer lines with F444W < 26.5 are indeterminate broad. However, we do not detect broad Balmer lines in RUBIES-UDS-28221, RUBIES-UDS-59971, RUBIES-UDS-853923, or RUBIES-UDS-977881 (the $z \sim 7$ quiescent galaxy from Weibel et al. 2025), despite full coverage.

spectroscopic sample with the public photometric catalogs from each study.

We begin with the selection of Kocevski et al. (2025), which performed double power-law fitting to HST and NIRCam photometry to select v-shaped SEDs. The exact filters used depend on the photometric redshift, but typically comprise three broadband filters both blue- and redward of the estimated Balmer limit. We identify 53 sources with matches to the RUBIES spectroscopy, 47 of which have robust $z_{spec} > 3.1$. The majority (65%) of these sources show broad Balmer emission lines, in line with an early estimate of the broad line fraction by Kocevski et al. (2025) that was based on a small fraction of the RUBIES dataset. Of the remaining 35%, two thirds are fainter sources where the presence of a broad line cannot be ruled out with the depth of the existing data, while the remainder suffer from data quality issues or lack G395M coverage of forbidden or Balmer lines.

This photometric sample spans a wide range in F444W magnitudes, and nearly half the sample is fainter than the RUBIES LRDs. For a representative analysis of the spectroscopic LRD recovery, we restrict our further comparison to sources brighter than F444W < 26.5. This limit is chosen based on the depth of the RUBIES PRISM spectra, corresponding to a median S/N ∼ 3 per resolution element for a well-centered point source (see de Graaff et al. 2025a). Correspondingly, we find that our v-shape selection is limited to similar magnitudes, where the PRISM spectra provide sufficient S/N for reliable continuum slope measurements. This magnitude limit also broadly applies to our broad-line detection method (see Table 1), though the effective limit in that case depends on additional factors such as line width, equivalent width, and the presence of narrow-line tracers like [O III]. This magnitude threshold thus sets a practical limit on the v-shape selection, and fainter LRDs–particularly those with broad or indeterminate lines–may remain underrepresented in our sample due to insufficient spectral sensitivity. Moreover, as described in Section 3.3.1 and shown in Figure 4, the distinction between genuine point sources and compact galaxies becomes increasingly ambiguous at these fainter magnitudes. We find that 21 of the total 34 spectroscopic LRDs satisfying this magnitude criterion are recovered by the selection of Kocevski et al. (2025). This translates to a success rate, i.e., a spectroscopic LRD completeness, of approximately 60%. We summarize these results in Table 1.

Next, we turn to the color-selected sample of Kokorev et al. (2024) which requires two red broadband colors at ∼2−4 µm as well as a single blue broadband color at <2 µm. Although photometric redshifts are not explicitly used, in practice these criteria translate to, and were optimized for, selection on rest-UV and rest-optical colors of high-redshift sources. We find 40 unique cross-matched sources, with 32 having robust $z_{spec} > 3.1$. This sample contains a remarkably high fraction of broad-line sources, 81%, corroborating the earlier finding of Greene et al. (2024) who evaluated the multi-color selection of Labbe et al. (2025) that is similar to that of Kokorev et al. (2024). The majority of the remaining 19% have indeterminate broad Balmer lines, i.e., lacking G395M coverage of either [O III] or H$\alpha$, or suffer from DQ issues, and the true broad line fraction may therefore be even higher. We find that 17 of the 34 RUBIES LRDs at F444W < 26.5 are recovered, which implies a spectroscopic LRD completeness of 50%.

Barro et al. (2024) apply a multi-color selection defined using the F115W, F200W, and F444W bands. These color criteria are informed by the redshifted tracks of a sample of five LRD SEDs spanning $z = 3-9$. Based on a catalog of 440 sources in the UDS and EGS that satisfy the criteria (Barro G., private communication) we find 101 unique cross-matched sources, 84 of which have $z_{spec} > 3.1$. The confirmed broad-line fraction, 60%, is lower than the other selection methods discussed so far. While this is primarily driven by faint, F444W < 26.5, or indeterminate broad sources, Barro et al. (2024) also selects four sources above our magnitude limit without data quality issues and full availability of relevant emission lines where we are

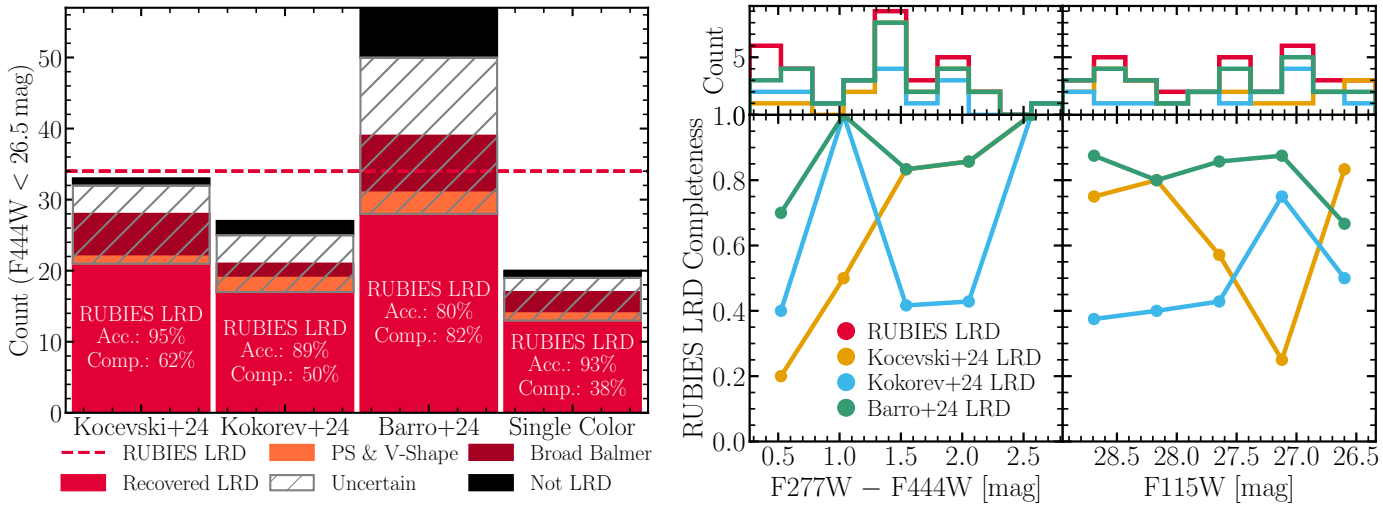


**Fig. 9.** Breakdown of photometric LRD selection methods at F444W < 26.5. The left panel shows how photometric LRDs are distributed among spectroscopically classified categories: spectroscopic LRDs (red), rest-optical point sources and v-shaped galaxies (orange), broad Balmer line sources (dark red), non-LRDs (black), and galaxies with unreliable feature measurements (gray hatched). Overall, photometric LRD selections are accurate but incomplete relative to spectroscopic identifications. The right panel investigates the completeness of the RUBIES photometric LRDs as a function of F277W−F444W color (left) and F115W magnitude (right). The top plots show histograms of RUBIES LRDs (red), matched LRDs from Kocevski et al. (2025, orange), and Kokorev et al. (2024, blue). The bottom plots display the binned completeness of each selection method relative to the RUBIES sample. We find that Kocevski et al. (2025) is incomplete at bluer colors, while Kokorev et al. (2024) is primarily incomplete at fainter rest-UV magnitudes.

unable to detect broad lines, including the $z \sim 7$ quiescent galaxy from Weibel et al. (2025), RUBIES-UDS-977881. This selection recovers the largest number of LRDs among the methods evaluated, identifying 28 of the 34 RUBIES sources in the magnitude-limited sample, corresponding to a completeness of 82%.

Finally, several studies have proposed the use of a single, extremely red rest-optical color to select LRDs (e.g., Akins et al. 2024; Barro et al. 2024; Greene et al. 2024). Multi-color selection has clear advantages, but it relies on the availability of a large number of photometric filters, which do not exist for the widest-area JWST programs such as COSMOS-Web or pure-parallel programs (e.g., Casey et al. 2023; Williams et al. 2025). Although not used before in the RUBIES fields, we also assess the use of the F277W−F444W color paired with our requirement of a dominant rest-optical point source (see Section 3.3). Following Akins et al. (2024), we first impose F277W−F444W > 1.5; due to the restrictive nature of this requirement it selects far fewer galaxies (29, of which 21 have robust $z_{\rm spec} > 3.1$). The broad line fraction among this sample is very high (78%; see Table 1); however, the recovery of spectroscopic LRDs is highly incomplete (38%) and the single-color selection thus performs significantly worse than the other photometric selections. If the color criterion is instead relaxed to F277W−F444W > 1.0 the LRD completeness improves (67%), but at the expense of the recovered broad line fraction, which drops to 64%.

### 5.2. Accuracy and contamination

The different photometric LRD selections are all successful in selecting sources with broad Balmer lines (upward of 65−80%), and select a large number of spectroscopic LRDs. This is perhaps not surprising in the context of our results of Section 4, where we demonstrated that a compact rest-optical morphology and v-shaped continuum are highly predictive of the presence of a broad line. However, unlike the spectroscopic v-shape measurements, the photometric colors and v-shapes can be biased by strong emission lines that substantially boost even broadband filters. So far, we have only focused on the success rates of broad line and LRD recovery. We now turn to the contaminants in these samples and the accuracy of the photometric selections.

To investigate the possible contaminants in the photometric samples, we first restrict our analysis to the magnitude-limited sample (F444W < 26.5). Whereas initial follow-up studies of LRDs highlighted brown dwarf stars in the Milky Way as possible interlopers (e.g., Langeroodi & Hjorth 2023; Burgasser et al. 2024; Greene et al. 2024), we find no such contaminants in the photometric samples, demonstrating the success of the color cuts that were imposed to filter out cool stars. In fact, even when expanding to the full sample we only find one faint brown dwarf in the sample selected by Kokorev et al. (2024) and Barro et al. (2024). The other likely class of contaminants consists of AGN or star-forming galaxies with high equivalent width emission lines, which bias the observed rest-optical colors measured from photometry, as demonstrated by Kocevski et al. (2023), Hainline et al. (2025), for example. However, we only identify one or two such sources in the magnitude-limited photometric samples, which are broad-line AGN with blue spectroscopic continua but very strong emission lines.

The sources for which we can confidently conclude that they are LRDs or contaminants therefore account for ~65% and ~5%, respectively, of the magnitude-limited photometric selections (see Table 1 and left panel of Figure 9). This still leaves a substantial fraction of sources of uncertain nature, which can be in equal parts ascribed to data quality issues preventing a robust broad-line measurement (e.g., chip gaps, lack of forbidden lines), and low-continuum S/N limiting a robust conclusion on whether the continuum is indeed v-shaped. To define the accuracy of the photometric LRD selections we therefore only consider the sources for which we can robustly determine both the broad line and continuum shape criteria. This spectroscopic LRD accuracy is very high (~90−95%) for the Kocevski et al. (2025), Kokorev et al. (2024), and single-color

photometric selections (as discussed in Section 5.1) and would still be high (∼80%) even in the extreme case that all uncertain sources without data quality issues are considered contamination. The Barro et al. (2024) sample, while more complete than the aforementioned selections, has a lower overall spectroscopic LRD accuracy of 80% with similar contaminants, i.e., blue broad-line AGN, as well as high-$z$ quiescent galaxies, such as RUBIES-UDS-977881 from Weibel et al. (2025).

Although the accuracy of the photometric LRD selection is very high, we emphasize that it only applies to the magnitude-limited sample of F444W < 26.5, and it is as of yet unclear how this would extend to the fainter LRD candidates. For these fainter candidates we may expect low-mass star-forming galaxies, i.e., compact sources with strong emission lines, to form a more prominent source of contamination. This is difficult to confirm or rule out with present data, as deep low- and medium-resolution spectra are needed to determine the broad-line and continuum properties. Perhaps even more challenging is the fact that lower-mass galaxies are increasingly compact and therefore difficult to distinguish from true point sources. This effect is especially pronounced in the F444W filter where, at the available depths in the UDS and EGS, the morphological classification must either become inaccurate or incomplete at F444W > 26.5 based on our fits to foreground stars.

### 5.3. Incompleteness

Most surprising is the fact that the photometric LRD selections are only able to recover up to 60% of the spectroscopic LRDs, even when restricting to F444W < 26.5. This high incompleteness impacts, for example, the inferred number densities and luminosity functions (e.g., Kocevski et al. 2025; Kokorev et al. 2024), and further increases the suggested tension between the inferred black hole properties and theoretical galaxy formation models (e.g., Habouzit 2025).

We investigate the origin of this incompleteness in the photometric samples in the right panel of Figure 9, which shows the spectroscopic LRD completeness as a function of the broad-band color F277W−F444W, a proxy for the rest-optical slope, and the F115W magnitude, tracing the rest-UV brightness. This enables us to identify the trade-offs made in each selection method and its impact on LRD completeness. The photometric v-shape selection of Kocevski et al. (2025) requires a strongly rising red rest-optical continuum, and additionally filters out sources that are likely to have strong emission lines based on the F277W−F356W and F277W−F410M colors. As a result, we find that the photometric v-shape selection of Kocevski et al. (2025) becomes increasingly incomplete toward bluer rest-optical colors. Relaxing the rest-optical color criteria would likely improve the completeness, but also would allow more extreme emission line galaxies with intrinsically blue continua to enter the sample. The multi-color selection of Kokorev et al. (2024) allows for more modest rest-optical colors, and the completeness is therefore approximately even across a wide range F277W−F444W color. However, Kokorev et al. (2024) imposed strict S/N criteria on the rest-UV (∼1−2 µm) magnitudes, which translates into an incompleteness predominantly at fainter rest-UV magnitudes. Lowering this rest-UV brightness threshold would likely increase the risk of contamination from red interlopers, such as brown dwarfs and compact dusty star-forming galaxies at lower redshifts.

Because these selection methods are incomplete in different regimes, it raises the question whether their combination would yield an improved sample. Indeed, we find only a modest overlap of 11 RUBIES LRDs between the Kocevski et al. (2025) and Kokorev et al. (2024) samples. The combination of the two samples therefore recovers 27 out of 34 spectroscopic LRDs in the magnitude limited sample, corresponding to a joint completeness of 79%. This high completeness is consistent with the findings of Barro et al. (2024), who showed that while the Kocevski et al. (2025) and Kokorev et al. (2024) selections overlap by only ∼50%, the Barro et al. (2024) method recovers nearly all sources selected by both. Our results confirm that this approach achieves broad recovery of spectroscopic LRDs with a completeness of 82% albeit at a compromised accuracy of 80%.

Nevertheless, a substantial fraction of the RUBIES LRDs remains unrecovered by all photometric selection methods. Our analysis has, thus far, neglected one crucial component that spectroscopy provides over photometry: robust redshifts. Redshift is used explicitly in the v-shape fitting of Kocevski et al. (2025) and implicitly enters the color selections of Kokorev et al. (2024) and Barro et al. (2024). These selections may therefore be influenced by uncertainties or systematics in photometric redshift estimation.

We evaluate the photometric redshift success for the robust $z_{\rm spec} > 3.1$ and spectroscopic LRD samples in the left panel of Figure 10. The reddest sources in RUBIES were selected without any initial photometric redshift constraint and therefore provide an ideal comparison sample. The photometric redshifts were obtained from template fitting to the cross-matched PSF-matched photometry from Weibel et al. (2024) with `eazy` (Brammer et al. 2008), using the `blue_sfhz_13` template set. Statistics are performed on the photometric redshift deviation: $\Delta = |\Delta z|/(1 + z_{\rm spec})$. We find that the photometric redshifts of the LRDs are slightly higher than the spectroscopic redshifts (median deviation of $\Delta_{\rm med} = 0.045$) when compared with little-to-no deviation in the RUBIES $z_{\rm spec} > 3.1$ sample ($\Delta_{\rm med} = -0.002$). Most importantly, we find a high outlier fraction $f_{\rm out} = 0.44$ (defined as $\Delta > 0.1$) and scatter ($\sigma_{\rm NMAD} = 0.127$), exceeding that of the full RUBIES spectroscopic sample by a factor two and three respectively ($f_{\rm out} = 0.19$ and scatter ($\sigma_{\rm NMAD} = 0.034$).

Indeed, we find that the photometric redshift outliers are preferentially excluded by the photometric selections. Of the fourteen photometric redshift outliers in the magnitude-limited LRD sample, Barro et al. (2024) recovers seven (50%), Kocevski et al. (2025) recovers six (41%), while Kokorev et al. (2024) recovers only one (14%). Notably, all spectroscopic LRDs missed by two or more selection methods are redshift outliers. Among these are sources with very strong Balmer breaks, such as RUBIES-UDS-154183 (*The Cliff*; de Graaff et al. 2025b) and RUBIES-UDS-144195, the latter having such a strong Balmer break that it is instead fit as a Lyman break at $z_{\rm phot} \sim 14$ (red triangle in Figure 10). Many of these strong break objects also demonstrate a turnover in the rest-optical and blue slopes at the reddest wavelengths. While our v-shape criteria selects them nonetheless, they may still miss more atypical or extreme cases. Although we find no such examples in our current sample, this remains a limitation of our color-based approach and may motivate broader selection strategies in future work.

Improving the completeness of future photometric selections will therefore require better treatment of the unusual colors of LRDs, which are currently not captured by commonly used template sets for photometric redshift fitting or not fully accounted for in the definition of color criteria. Recently, a dedicated LRD template was introduced in `eazy`, which was constructed from the LRD spectrum of Killi et al. (2024) combined with a hot dusty torus model that rises sharply in the near- to mid-infrared. We also test the inclusion of this template (`agn_blue_sfhz_13`)

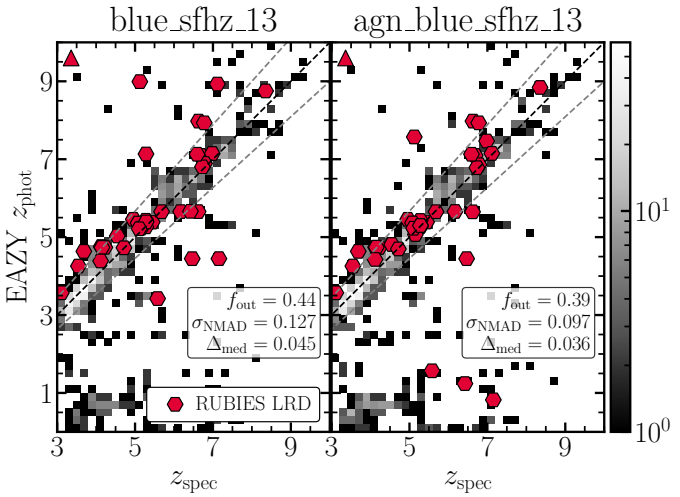


**Fig. 10.** Best-fit photometric vs. spectroscopic redshift for RUBIES sources with robust $z_{\rm spec} > 3.1$ (gray histogram) and the LRD sample (red hexagons; triangle indicates out of plot). Photometric redshifts were measured using `eazy` (Brammer et al. 2008) with two different template sets: the `blue_sfhz_13` set optimized for high-redshift galaxies (left) and the `agn_blue_sfhz_13` set which includes an AGN template constructed from the LRD of Killi et al. (2024) and a torus model (right). The dashed lines show $|\Delta z|/(1+z_{\rm spec}) = 0.1$. Although including this AGN template reduces the number of outliers and photometric redshift scatter for the LRD sample, a small bias toward higher photometric redshifts remains.

in the right panel Figure 10, and find that it sightly improves outlier fraction ($f_{\rm out} = 0.39$), scatter ($\sigma_{\rm NMAD} = 0.097$), and median deviation ($\Delta_{\rm med} = 0.036$)[3]. However, we note that a typical torus model may fail to properly describe LRDs as many have shown to have flat mid-IR colors not well described by hot dust (Williams et al. 2024; Setton et al. 2025; Wang et al. 2025; de Graaff et al. 2025b; Chen et al. 2025a).

The success of photometric LRD selection hinges on accurately capturing their unique spectral properties. Although current methods achieve high accuracy in identifying LRDs, their incompleteness underscores the limitations of relying solely on broadband photometry. The high photometric redshift outlier fraction of spectroscopic LRDs, particularly among LRDs missed by both v-shaped and multi-color selection methods, suggests that standard high-redshift galaxy or AGN templates fail to fully describe LRD SEDs. In the future, developing new empirical LRD templates and combining complementary selection criteria may maximize photometric LRD completeness. Large spectroscopic campaigns like RUBIES will be essential to validate such photometric selections across the full color-morphology parameter space. Crucially, the simplicity of the RUBIES selection function, based primarily on a color–magnitude criterion without morphological pre-selection, enables the computation of completeness corrections across galaxy colors. While RUBIES is complete for the reddest sources, the survey also prioritizes the brightest sources and selects a large number of blue sources due to their relative abundance, ensuring that this study still recovers broad-line and LRD systems across the full color space.

[3] We caution that the opposite is true for the general population of RUBIES sources, as $\Delta = -0.003$, $\sigma_{\rm NMAD} = 0.037$ and $f_{\rm out} = 0.18$ are all slightly worse than for the fits without an LRD template.

## 6. Summary

We used the large spectroscopic dataset of JWST program RUBIES to quantify the characteristics commonly associated with LRDs – broad Balmer emission, v-shaped continua, point-like rest-optical morphologies – among the high-redshift galaxy population. Because the RUBIES targets span a wide range in color and redshift without any morphological pre-selection, they are uniquely positioned to determine the prevalence of each LRD characteristic across the galaxy population.

We presented one of the largest spectroscopic samples of broad Balmer line sources at high redshift to date, including 80 robust detections at $z > 3.1$, of which 28 (35%) lie at $z > 6$. Our detections are enabled by the `unite` package, which combines multiple NIRSpec spectra, i.e., the PRISM and G395M spectra, simultaneously to model emission lines and continua. This approach leverages the signal-to-noise ratio of the PRISM and the resolution of G395M to identify kinematic components of emission lines, overcoming limitations of single-disperser analyses.

Moreover, we used the RUBIES spectra to measure v-shaped continua, and measure detailed morphologies from NIRCam imaging to determine which sources are point-source dominated in the rest-optical. Remarkably, the definition of an LRD emerges naturally from the measured spectroscopic and photometric features: all point sources with (spectroscopic) v-shaped continua exhibit broad Balmer lines where the data quality permits detection. This strongly suggests that these three features are not coincidental, but likely stem from a common physical origin. This can possibly be explained in the context of the recently proposed phenomenon of a massive accreting black hole embedded in an envelope of dense gas (Inayoshi & Maiolino 2025; Ji et al. 2025; Naidu et al. 2025; de Graaff et al. 2025b; Kido et al. 2025; Taylor et al. 2025b).

In detail, our primary findings can be summarized as follows:

1. The sample of broad Balmer line sources span a wide range in rest-optical broadband photometric colors, but are typically redder than the full RUBIES sample at $z > 3.1$ due to a combination of red rest-optical continua and high equivalent width emission lines.
2. The majority of sources with (spectroscopic) v-shaped continua also show a dominant point source component at rest-optical wavelengths. Remarkably, we robustly detect broad Balmer emission lines for upward of 80% of these sources; the remainder are inconclusive primarily due to data shortcomings. Similarly, the majority of sources with v-shaped continua show broad Balmer emission lines. Of this population, 80% also show a prominent point-source component in rest-optical imaging.
3. Strikingly, a population of sources with all three features emerges naturally from the data, and we therefore define this sample as spectroscopic LRDs, constituting the largest such sample (36) to date. Compared to the full sample of broad Balmer line sources, spectroscopic LRDs are the most luminous H$\alpha$ emitters at any $M_{\rm UV}$.
4. Photometric LRD selections are highly accurate in their recovery of broad Balmer line sources (65–80%), as well as spectroscopic LRDs (up to ~95% for F444W $< 26.5$). However, only 50–80% of the RUBIES LRDs were previously identified in these photometric searches, with higher completeness coming at the cost of LRD accuracy. In particular, the selections are increasingly incomplete for bluer broadband rest-optical colors and fainter UV magnitudes.
5. Combining multiple photometric LRD selections improves completeness but still leaves a large fraction of LRDs

unrecovered. Sources that were missed typically have highly uncertain photometric redshifts and/or very strong Balmer breaks. This highlights the need for more nuanced photometric selection criteria as well as large spectroscopic surveys such as RUBIES.

With a clear definition of the spectro-photometric properties that select LRDs, we are now able to build a large robust sample of LRDs within RUBIES and the broader JWST spectroscopic archive. We can then begin to examine their detailed properties, such as the prevalence of Balmer absorption features and Balmer breaks, across the entire LRD population. In turn, this will provide critical clues about the evolutionary stages or environmental conditions of these systems, enabling a clearer understanding of their role in galaxy evolution and black hole growth.

## Data availability

Full Table B.1 is available at the CDS via https://cdsarc.cds.unistra.fr/viz-bin/cat/J/A+A/702/A57

*Acknowledgements.* We would like to thank the anonymous reviewer for their constructive comments which improved the final manuscript. REH acknowledges support by the German Aerospace Center (DLR) and the Federal Ministry for Economic Affairs and Energy (BMWi) through program 50OR2403 'RUBIES'. TBM was supported by a CIERA Postdoctoral Fellowship. This work used computing resources provided by Northwestern University and the Center for Interdisciplinary Exploration and Research in Astrophysics (CIERA). This research was supported in part through the computational resources and staff contributions provided for the Quest high performance computing facility at Northwestern University which is jointly supported by the Office of the Provost, the Office for Research, and Northwestern University Information Technology. Support for this work was provided by The Brinson Foundation through a Brinson Prize Fellowship grant. The Cosmic Dawn Center is funded by the Danish National Research Foundation (DNRF) under grant #140. This work has received funding from the Swiss State Secretariat for Education, Research and Innovation (SERI) under contract number MB22.00072, as well as from the Swiss National Science Foundation (SNSF) through project grant 200020_207349. Support for this work for RPN was provided by NASA through the NASA Hubble Fellowship grant HST-HF2-51515.001-A awarded by the Space Telescope Science Institute, which is operated by the Association of Universities for Research in Astronomy, Incorporated, under NASA contract NAS5-26555. The work of CCW is supported by NOIRLab, which is managed by the Association of Universities for Research in Astronomy (AURA) under a cooperative agreement with the National Science Foundation. The data products presented herein were retrieved from the Dawn JWST Archive (DJA). DJA is an initiative of the Cosmic Dawn Center (DAWN). This work is based in part on observations made with the NASA/ESA/CSA James Webb Space Telescope. The data were obtained from the Mikulski Archive for Space Telescopes at the Space Telescope Science Institute, which is operated by the Association of Universities for Research in Astronomy, Inc., under NASA contract NAS 5-03127 for JWST. These observations are associated with programs numbers 1345, 1837, 2234, 2279, 2514, 2750, 3990 and 4233. Support for program no. 4233 was provided by NASA through a grant from the Space Telescope Science Institute, which is operated by the Association of Universities for Research in Astronomy, Inc., under NASA contract NAS 5-03127. The authors acknowledge the CEERS, PRIMER, PANORAMIC, and BEACONS teams for developing their observing program with a zero-exclusive-access period. We acknowledge the use of the following software packages which were instrumental in the development of this work: `Astropy` (Astropy Collaboration 2013, 2018, 2022), `grizli` (Brammer 2023a), `jax` (Bradbury et al. 2018), `jwst` (Bushouse et al. 2022), LaTeX (Lamport 1994), `Matplotlib` (Hunter 2007), `msaexp` (Brammer 2023b), `msafit` (de Graaff et al. 2024), `NumPy` (Oliphant 2006; van der Walt et al. 2011; Harris et al. 2020), `NumPyro` (Phan et al. 2019), `photutils` (Bradley et al. 2024b), `pysersic` (Pasha & Miller 2023), `photutils` (Bradley et al. 2024a), `sedpy` (Johnson 2021), `Source-Extractor` (Bertin & Arnouts 1996), and `unite` (Hviding 2025). This work makes use of color palettes created by Martin Krzywinski designed for colorblindness. The color palettes and more information can be found at http://mkweb.bcgsc.ca/colorblind/

## References

Akins, H. B., Casey, C. M., Allen, N., et al. 2023, ApJ, 956, 61
Akins, H. B., Casey, C. M., Lambrides, E., et al. 2024, ApJ, submitted [arXiv:2406.10341]
Astropy Collaboration (Robitaille, T. P., et al.) 2013, A&A, 558, A33
Astropy Collaboration (Price-Whelan, A. M., et al.) 2018, AJ, 156, 123
Astropy Collaboration (Price-Whelan, A. M., et al.) 2022, ApJ, 935, 167
Baggen, J. F. W., van Dokkum, P., Labbé, I., et al. 2023, ApJ, 955, L12
Baggen, J. F. W., van Dokkum, P., Brammer, G., et al. 2024, ApJ, 977, L13
Bagley, M. B., Finkelstein, S. L., Koekemoer, A. M., et al. 2023, ApJ, 946, L12
Barro, G., Pérez-González, P. G., Kocevski, D. D., et al. 2024, ApJ, 963, 128
Bertin, E., & Arnouts, S. 1996, A&AS, 117, 393
Bezanson, R., Labbe, I., Whitaker, K. E., et al. 2024, ApJ, 974, 92
Boylan-Kolchin, M. 2023, Nat. Astron., 7, 731
Bradbury, J., Frostig, R., Hawkins, P., et al. 2018, JAX: Composable Transformations of Python+NumPy Programs
Bradley, L., Sipőcz, B., Robitaille, T., et al. 2024a, https://doi.org/10.5281/zenodo.12585239
Bradley, L., Sipőcz, B., Robitaille, T., et al. 2024b, https://doi.org/10.5281/zenodo.13989456
Brammer, G. 2023a, https://doi.org/10.5281/zenodo.1146904
Brammer, G. 2023b, https://doi.org/10.5281/zenodo.8319596
Brammer, G. B., van Dokkum, P. G., & Coppi, P. 2008, ApJ, 686, 1503
Brammer, G. B., van Dokkum, P. G., Franx, M., et al. 2012, ApJS, 200, 13
Burgasser, A. J., Bezanson, R., Labbe, I., et al. 2024, ApJ, 962, 177
Bushouse, H., Eisenhamer, J., Dencheva, N., et al. 2022, https://doi.org/10.5281/zenodo.7229890
Carnall, A. C., Cullen, F., McLure, R. J., et al. 2024, MNRAS, 534, 325
Casey, C. M., Kartaltepe, J. S., Drakos, N. E., et al. 2023, ApJ, 954, 31
Chen, K., Li, Z., Inayoshi, K., Ho, L. C., et al. 2025a, ArXiv e-prints [arXiv:2505.22600]
Chen, C.-H., Ho, L. C., Li, R., & Zhuang, M.-Y. 2025b, ApJ, 983, 60
Cooper, O. R., Brammer, G., Heintz, K. E., et al. 2025, ApJ, 982, 125
de Graaff, A., Rix, H.-W., Carniani, S., et al. 2024, A&A, 684, A87
de Graaff, A., Brammer, G., Weibel, A., et al. 2025a, A&A, 697, A189
de Graaff, A., Rix, H. W., Naidu, R. P., et al. 2025b, A&A, 701, A168
Donnan, C. T., McLure, R. J., Dunlop, J. S., et al. 2024, MNRAS, 533, 3222
Finkelstein, S. L., Bagley, M. B., Arrabal Haro, P., et al. 2025, ApJ, 983, L4
Förster Schreiber, N. M., Übler, H., Davies, R. L., et al. 2019, ApJ, 875, 21
Furtak, L. J., Zitrin, A., Plat, A., et al. 2023, ApJ, 952, 142
Furtak, L. J., Labbé, I., Zitrin, A., et al. 2024, Nature, 628, 57
Galavis, M. E., Mendoza, C., & Zeippen, C. J. 1997, A&AS, 123, 159
Gardner, J. P., Mather, J. C., Abbott, R., et al. 2023, PASP, 135, 068001
Gibson, J. L., Nelson, E., Williams, C. C., et al. 2024, ApJ, 974, 48
Greene, J. E., Labbe, I., Goulding, A. D., et al. 2024, ApJ, 964, 39
Grogin, N. A., Kocevski, D. D., Faber, S. M., et al. 2011, ApJS, 197, 35
Grudić, M. Y., Hopkins, P. F., Quataert, E., & Murray, N. 2019, MNRAS, 483, 5548
Guia, C. A., Pacucci, F., & Kocevski, D. D. 2024, RNAAS, 8, 207
Habouzit, M. 2025, MNRAS, 537, 2323
Hainline, K. N., Helton, J. M., Johnson, B. D., et al. 2024, ApJ, 964, 66
Hainline, K. N., Maiolino, R., Juodžbalis, I., et al. 2025, ApJ, 979, 138
Hao, L., Strauss, M. A., Fan, X., et al. 2005, AJ, 129, 1795
Harikane, Y., Zhang, Y., Nakajima, K., et al. 2023, ApJ, 959, 39
Harris, C. R., Millman, K. J., van der Walt, S. J., et al. 2020, Nature, 585, 357
Heintz, K. E., Brammer, G. B., Watson, D., et al. 2025, A&A, 693, A60
Hoffman, M. D., & Gelman, A. 2014, J. Mach. Learn. Res., 15, 1593
Hopkins, P. F., Murray, N., Quataert, E., & Thompson, T. A. 2010, MNRAS, 401, L19
Hunter, J. D. 2007, Comput. Sci. Eng., 9, 90
Hviding, R. E. 2025, https://doi.org/10.5281/zenodo.15585035
Hviding, R., de Graaff, A., Setton, D., Miller, T., & Greene, J. 2025, https://doi.org/10.5281/zenodo.15528783
Inayoshi, K., & Maiolino, R. 2025, ApJ, 980, L27
Ji, X., Maiolino, R., Übler, H., et al. 2025, MNRAS, submitted [arXiv:2501.13082]
Johnson, B. D. 2021, https://doi.org/10.5281/zenodo.4582723
Juodžbalis, I., Maiolino, R., Baker, W. M., et al. 2025, MNRAS, submitted [arXiv:2504.03551]
Kido, D., Ioka, K., Hotokezaka, K., Inayoshi, K., & Irwin, C. M. 2025, MNRAS, submitted [arXiv:2505.06965]
Killi, M., Watson, D., Brammer, G., et al. 2024, A&A, 691, A52
Kocevski, D. D., Onoue, M., Inayoshi, K., et al. 2023, ApJ, 954, L4
Kocevski, D. D., Finkelstein, S. L., Barro, G., et al. 2025, ApJ, 986, 126
Koekemoer, A. M., Faber, S. M., Ferguson, H. C., et al. 2011, ApJS, 197, 36
Kokorev, V., Fujimoto, S., Labbe, I., et al. 2023, ApJ, 957, L7
Kokorev, V., Caputi, K. I., Greene, J. E., et al. 2024, ApJ, 968, 38
Labbé, I., van Dokkum, P., Nelson, E., et al. 2023, Nature, 616, 266
Labbe, I., Greene, J. E., Matthee, J., et al. 2024, ApJ, submitted [arXiv:2412.04557]

Labbe, I., Greene, J. E., Bezanson, R., et al. 2025, ApJ, 978, 92
Lamport, L. 1994, LaTeX: A Document Preparation System, 2nd edn. (Addison-Wesley Professional)
Langeroodi, D., & Hjorth, J. 2023, ApJ, 957, L27
Larson, R. L., Finkelstein, S. L., Kocevski, D. D., et al. 2023, ApJ, 953, L29
Leung, G. C. K., Coil, A. L., Aird, J., et al. 2019, ApJ, 886, 11
Li, J., Silverman, J. D., Shen, Y., et al. 2025, ApJ, 981, 19
Lin, X., Wang, F., Fan, X., et al. 2024, ApJ, 974, 147
Lin, X., Fan, X., Wang, F., et al. 2025, ApJ, submitted [arXiv:2504.08039]
Ma, Y., Greene, J. E., Setton, D. J., et al. 2025, ApJ, 981, 191
Maiolino, R., Scholtz, J., Curtis-Lake, E., et al. 2024, A&A, 691, A145
Matthee, J., Naidu, R. P., Brammer, G., et al. 2024, ApJ, 963, 129
Naidu, R. P., Matthee, J., Kramarenko, I., et al. 2024, Open J. Astrophys., submitted [arXiv:2410.01874]
Naidu, R. P., Matthee, J., Katz, H., et al. 2025, Nature, submitted [arXiv:2503.16596]
Oke, J. B., & Gunn, J. E. 1983, ApJ, 266, 713
Oliphant, T. E. 2006, A Guide to NumPy (USA: Trelgol Publishing), 1
Pasha, I., & Miller, T. B. 2023, JOSS, 8, 5703
Pérez-González, P. G., Barro, G., Annunziatella, M., et al. 2023, ApJ, 946, L16
Pérez-González, P. G., Barro, G., Rieke, G. H., et al. 2024, ApJ, 968, 4
Phan, D., Pradhan, N., & Jankowiak, M. 2019, ArXiv e-prints [arXiv:1912.11554]
Pizzati, E., Hennawi, J. F., Schaye, J., et al. 2025, MNRAS, 539, 2910
Rinaldi, P., Bonaventura, N., Rieke, G. H., et al. 2024, ApJ, submitted [arXiv:2411.14383]
Rusakov, V., Watson, D., Nikopoulos, G. P., et al. 2025, Nature, submitted [arXiv:2503.16595]
Setton, D. J., Greene, J. E., de Graaff, A., et al. 2024, ApJ, submitted [arXiv:2411.03424]
Setton, D. J., Greene, J. E., Spilker, J. S., et al. 2025, ApJ, submitted [arXiv:2503.02059]
Skelton, R. E., Whitaker, K. E., Momcheva, I. G., et al. 2014, ApJS, 214, 24
Sun, F., Fudamoto, Y., Lin, X., et al. 2025, ApJS, submitted [arXiv:2503.15587]
Taylor, A. J., Finkelstein, S. L., Kocevski, D. D., et al. 2025a, ApJ, 986, 165
Taylor, A. J., Kokorev, V., Kocevski, D. D., et al. 2025b, ApJ, accepted [arXiv:2505.04609]
Valentino, F., Brammer, G., Gould, K. M. L., et al. 2023, ApJ, 947, 20
van der Walt, S., Colbert, S. C., & Varoquaux, G. 2011, Comput. Sci. Eng., 13, 22
Wang, B., Leja, J., de Graaff, A., et al. 2024, ApJ, 969, L13
Wang, B., de Graaff, A., Davies, R. L., et al. 2025, ApJ, 984, 121
Watanabe, S., & Opper, M. 2010, J. Mach. Learn. Res., 11, 1243
Weibel, A., Oesch, P. A., Barrufet, L., et al. 2024, MNRAS, 533, 1808
Weibel, A., de Graaff, A., Setton, D. J., et al. 2025, ApJ, 983, 11
Williams, C. C., Alberts, S., Ji, Z., et al. 2024, ApJ, 968, 34
Williams, C. C., Oesch, P. A., Weibel, A., et al. 2025, ApJ, 979, 140
Xiao, M., Williams, C. C., Oesch, P. A., et al. 2025, A&A, 696, A156
Zhuang, M. Y., Li, J., Shen, Y., et al. 2025, ApJ, submitted [arXiv:2505.20393]

## Appendix A: LRDs from RUBIES

We present all spectroscopically identified LRDs from RUBIES, along with all v-shaped and unresolved sources where we are unable to identify broad lines due to data quality limitations. We identify a total of 36 spectroscopic LRDs and seven additional sources with v-shaped continua and dominant rest-optical point sources. In Figure A.1 we present the color images (constructed from the F444W, F277W and F150W NIRCam filters), PRISM spectra, and G395M zoom-ins of the H$\alpha$ broad emission for all 43 objects. Key properties of spectroscopic LRDs and unresolved v-shaped galaxies are provided in Tables A.1 and A.2 respectively. We caution that the reported broad Balmer FWHM values are derived from Gaussian fitting with FWHM $< 2500\,\mathrm{km\,s^{-1}}$ that may not best represent the spectral profile. In Table A.2 we also include the reason why each unresolved v-shaped galaxy has an indeterminate broad line, i.e., due to a DQ issue or missing forbidden or Balmer line.

**Table A.1.** RUBIES spectroscopic LRDs

| Field | ID | R.A. | Dec | $z_{\rm spec}$ [a] | ΔWAIC | Broad FWHM [b] | $\beta_{\rm UV}$ | $\beta_{\rm opt.}$ | F444W [c] |
|---|---|---|---|---|---|---|---|---|---|
| | | J2000 | | | | $\mathrm{km\,s^{-1}}$ | | | mag |
| UDS | 40579 | 34.244200 | −5.245871 | 3.11 | 84 | 2466 ± 31 | −0.37 ± 0.02 | 1.97 ± 0.10 | 21.95 |
| UDS | 144195 | 34.325156 | −5.143685 | 3.36 | 143 | 2053 ± 130 | −1.52 ± 0.08 | 0.64 ± 0.02 | 24.52 |
| UDS | 154183 | 34.410749 | −5.129664 | 3.55 | 367 | 2481 ± 18 | −0.69 ± 0.07 | 1.12 ± 0.01 | 23.23 |
| UDS | 23438 | 34.338271 | −5.280895 | 3.69 | 69 | 2058 ± 183 | −1.79 ± 0.04 | 0.64 ± 0.05 | 24.71 |
| UDS | 167741 | 34.334603 | −5.110269 | 4.12 | 25 | 2399 ± 99 | −1.88 ± 0.04 | 0.66 ± 0.19 | 24.69 |
| UDS | 31747 | 34.223757 | −5.260245 | 4.13 | 98 | 2277 ± 150 | −0.91 ± 0.19 | 0.85 ± 0.01 | 24.80 |
| UDS | 119957 | 34.268908 | −5.176722 | 4.15 | 194 | 1978 ± 89 | −1.66 ± 0.06 | 0.91 ± 0.03 | 25.40 |
| EGS | 28812 | 214.924149 | 52.849050 | 4.22 | 841 | 2194 ± 60 | −0.61 ± 0.08 | 1.04 ± 0.03 | 24.47 |
| EGS | 29489 | 215.022071 | 52.920786 | 4.54 | 207 | 2370 ± 85 | −1.63 ± 0.13 | 0.80 ± 0.10 | 25.84 |
| UDS | 182791 | 34.213813 | −5.087050 | 4.72 | 1123 | 2496 ± 4 | −1.23 ± 0.01 | 0.43 ± 0.03 | 24.86 |
| EGS | 42232 | 214.886792 | 52.855381 | 4.95 | 393 | 2449 ± 40 | −1.00 ± 0.07 | 0.42 ± 0.03 | 22.74 |
| EGS | 61496 | 214.972441 | 52.962192 | 5.08 | 40 | 1509 ± 173 | −1.06 ± 0.07 | 0.89 ± 0.04 | 25.82 |
| EGS | 952625 | 214.975529 | 52.925268 | 5.11 | 28 | 1367 ± 337 | −1.71 ± 0.37 | 2.31 ± 0.31 | 26.40 |
| UDS | 830237 | 34.374852 | −5.275529 | 5.12 | 57 | 1238 ± 214 | −2.50 ± 0.13 | 0.96 ± 0.26 | 26.53 |
| UDS | 149298 | 34.424311 | −5.136491 | 5.15 | 65 | 2120 ± 248 | −1.07 ± 0.03† | 3.41 ± 0.60 | 24.23 |
| UDS | 53692 | 34.455376 | −5.231814 | 5.28 | 43 | 1725 ± 301 | −2.25 ± 0.43 | 1.46 ± 0.09 | 26.26 |
| EGS | 42046 | 214.795368 | 52.788847 | 5.28 | 4558 | 2499 ± 1 | −0.23 ± 0.01 | 0.65 ± 0.03 | 23.16 |
| UDS | 970351 | 34.261900 | −5.105205 | 5.28 | 51 | 2396 ± 91 | −0.84 ± 0.07† | 0.76 ± 0.05 | 25.64 |
| EGS | 926125 | 215.137081 | 52.988554 | 5.28 | 1426 | 1949 ± 57 | −1.09 ± 0.04 | 1.93 ± 0.05 | 25.26 |
| UDS | 29813 | 34.453355 | −5.270717 | 5.44 | 477 | 2245 ± 101 | −2.27 ± 0.13 | 0.98 ± 0.08 | 25.80 |
| UDS | 172350 | 34.368951 | −5.103941 | 5.58 | 592 | 1922 ± 46 | −1.36 ± 0.04 | 0.37 ± 0.02 | 24.57 |
| EGS | 37124 | 214.990977 | 52.916524 | 5.68 | 145 | 2453 ± 44 | −2.03 ± 0.26† | 0.80 ± 0.01 | 25.13 |
| UDS | 50716 | 34.313154 | −5.226781 | 6.17 | 61 | 2250 ± 159 | −1.61 ± 0.12 | 2.25 ± 0.13 | 25.80 |
| UDS | 57040 | 34.470042 | −5.238069 | 6.42 | 1567 | 2290 ± 34 | −0.84 ± 0.20 | 0.72 ± 0.01 | 24.07 |
| UDS | 36171 | 34.345003 | −5.260115 | 6.47 | 16 | 2177 ± 261 | −1.78 ± 0.35 | 0.46 ± 0.08 | 26.09 |
| UDS | 967770 | 34.228526 | −5.101526 | 6.59 | 13 | 2330 ± 145 | −1.82 ± 0.13 | 0.36 ± 0.05 | 26.04 |
| EGS | 53254 | 214.797537 | 52.818746 | 6.62 | 64 | 2067 ± 303 | −1.33 ± 0.01† | 0.71 ± 0.23 | 25.73 |
| UDS | 33938 | 34.266442 | −5.256391 | 6.63 | 32 | 1143 ± 297 | −1.87 ± 0.09 | 0.98 ± 0.26 | 26.71 |
| EGS | 49140 | 214.892248 | 52.877410 | 6.68 | 5279 | 2499 ± 1 | −0.69 ± 0.01 | 1.10 ± 0.02 | 23.92 |
| EGS | 948917 | 214.892479 | 52.856890 | 6.73 | 292 | 2217 ± 134 | −1.21 ± 0.01 | 0.86 ± 0.02 | 25.50 |
| UDS | 807469 | 34.376139 | −5.310366 | 6.78 | 788 | 1742 ± 74 | −1.13 ± 0.39† | 2.48 ± 0.35 | 25.03 |
| EGS | 927271 | 215.078259 | 52.948497 | 6.78 | 19 | 1649 ± 357 | −1.64 ± 0.02 | 0.91 ± 0.09 | 26.19 |
| EGS | 55604 | 214.983026 | 52.956001 | 6.98 | 6966 | 2499 ± 1 | −0.96 ± 0.01 | 1.50 ± 0.02 | 23.82 |
| UDS | 848745 | 34.310575 | −5.249898 | 7.11 | 86 | 1735 ± 292 | −1.12 ± 0.08 | 1.72 ± 0.13 | 26.11 |
| EGS | 42803 | 214.929524 | 52.887919 | 7.15 | 237 | 2393 ± 78 | −1.19 ± 0.11 | 1.67 ± 0.04 | 26.04 |
| EGS | 966323 | 214.876149 | 52.880831 | 8.35 | 55 | 2199 ± 223 | −1.13 ± 0.01 | 0.57 ± 0.07 | 25.68 |

**Notes.** The machine-readable version of this table is available on Zenodo (Hviding et al. 2025).
[a]Based on the best DJA value.
[b]We caution that these values are derived from Gaussian fitting with FWHM $< 2500\,\mathrm{km\,s^{-1}}$ that may not best represent the spectral profile.
[c]Obtained from the Weibel et al. (2024) catalogs.
†$\beta_{\rm UV}$ derived from photometry.

**Table A.2.** RUBIES v-shaped rest-optical point sources (with indeterminate broad Balmer emission)

| Field | ID | R.A. | Dec | $z_{spec}$[a] | Broad H I Note | $\beta_{UV}$ | $\beta_{opt.}$ | F444W[b] |
|---|---|---|---|---|---|---|---|---|
| | | J2000 | | | | | | mag |
| UDS | 176292 | 34.228100 | −5.098144 | 3.14 | Edge of Range | −2.58 ± 0.86 | 1.48 ± 0.09 | 25.27 |
| UDS | 16053 | 34.367104 | −5.293524 | 3.95 | No [O III] | −1.37 ± 0.40 | 0.60 ± 0.05 | 25.50 |
| UDS | 147411 | 34.360718 | −5.139081 | 3.97 | No [O III] | −1.24 ± 0.08 | 0.17 ± 0.05 | 26.29 |
| UDS | 40800 | 34.324122 | −5.252789 | 4.98 | H$\beta$ & [O III] DQ | −2.51 ± 0.98[†] | 2.52 ± 0.25 | 26.67 |
| EGS | 69475 | 214.949187 | 52.964143 | 5.62 | No H$\alpha$ | −1.73 ± 0.03 | 0.37 ± 0.09 | 25.76 |
| UDS | 928474 | 34.243700 | −5.271438 | 6.93 | Contamination | −2.28 ± 0.22 | 1.55 ± 0.22 | 26.20 |
| EGS | 932920 | 214.927819 | 52.850001 | 7.48 | No H$\alpha$ | −1.97 ± 0.01 | 0.69 ± 0.14 | 26.69 |

**Notes.** The machine-readable version of this table is available on Zenodo (Hviding et al. 2025).
[a]Based on the best DJA value.
[b]Obtained from the Weibel et al. (2024) catalogs.
[†]$\beta_{UV}$ derived from photometry.

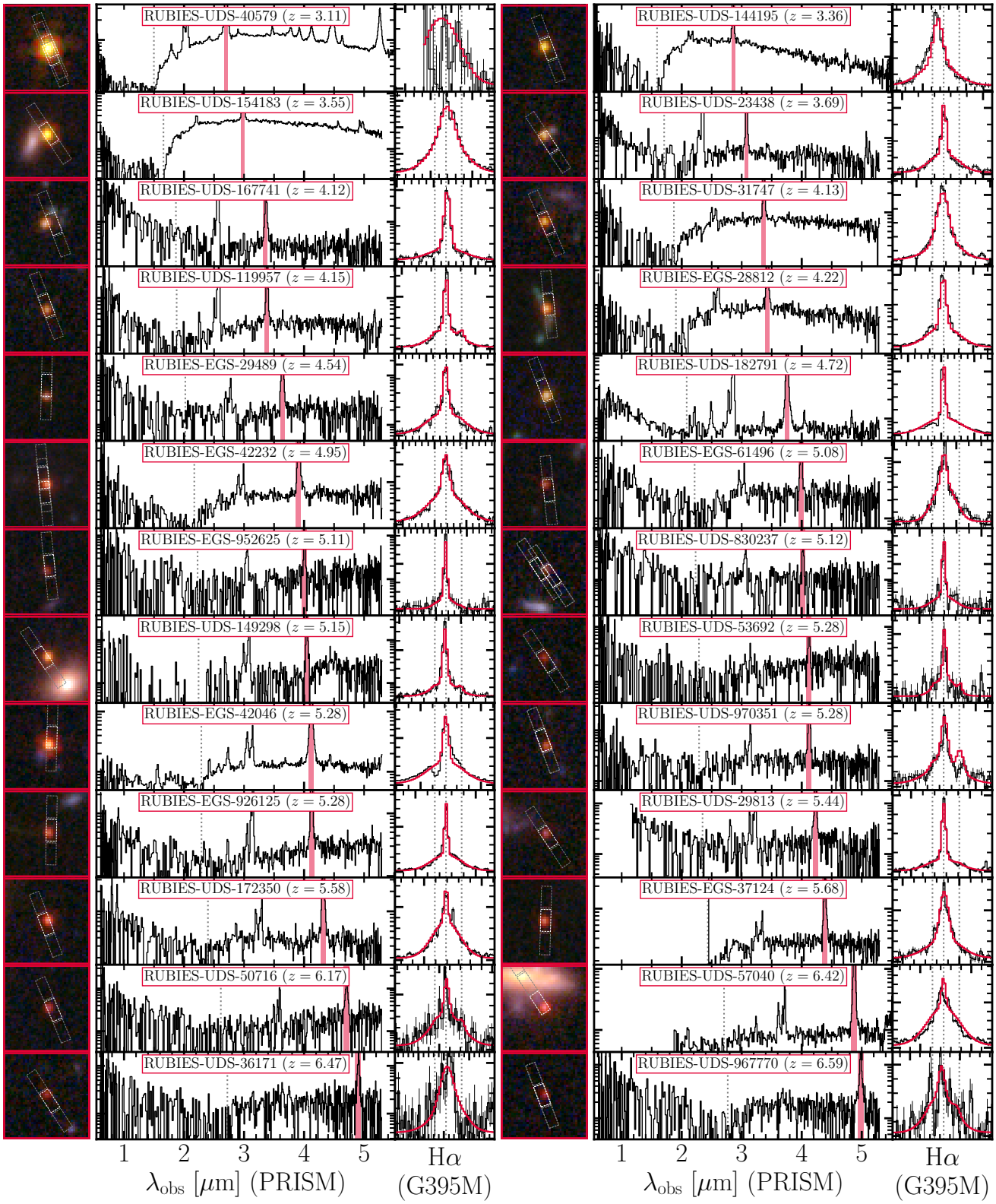


**Fig. A.1.** All RUBIES LRDs (red) found in this work followed by rest-optical point sources with v-shaped continua (orange) all organized by redshift. In each column in each row we show the following: the 1″×1″ F444W/F277W/F150W RGB cutouts (left), the log-scaled PRISM spectra with the location of the Balmer limit marked with a dashed line (middle), and the linear-scaled G395M ±3000 km s$^{-1}$ zoom-in of the H$\alpha$ line where available, otherwise H$\beta$, with the broad `unite` fit superimposed (right).

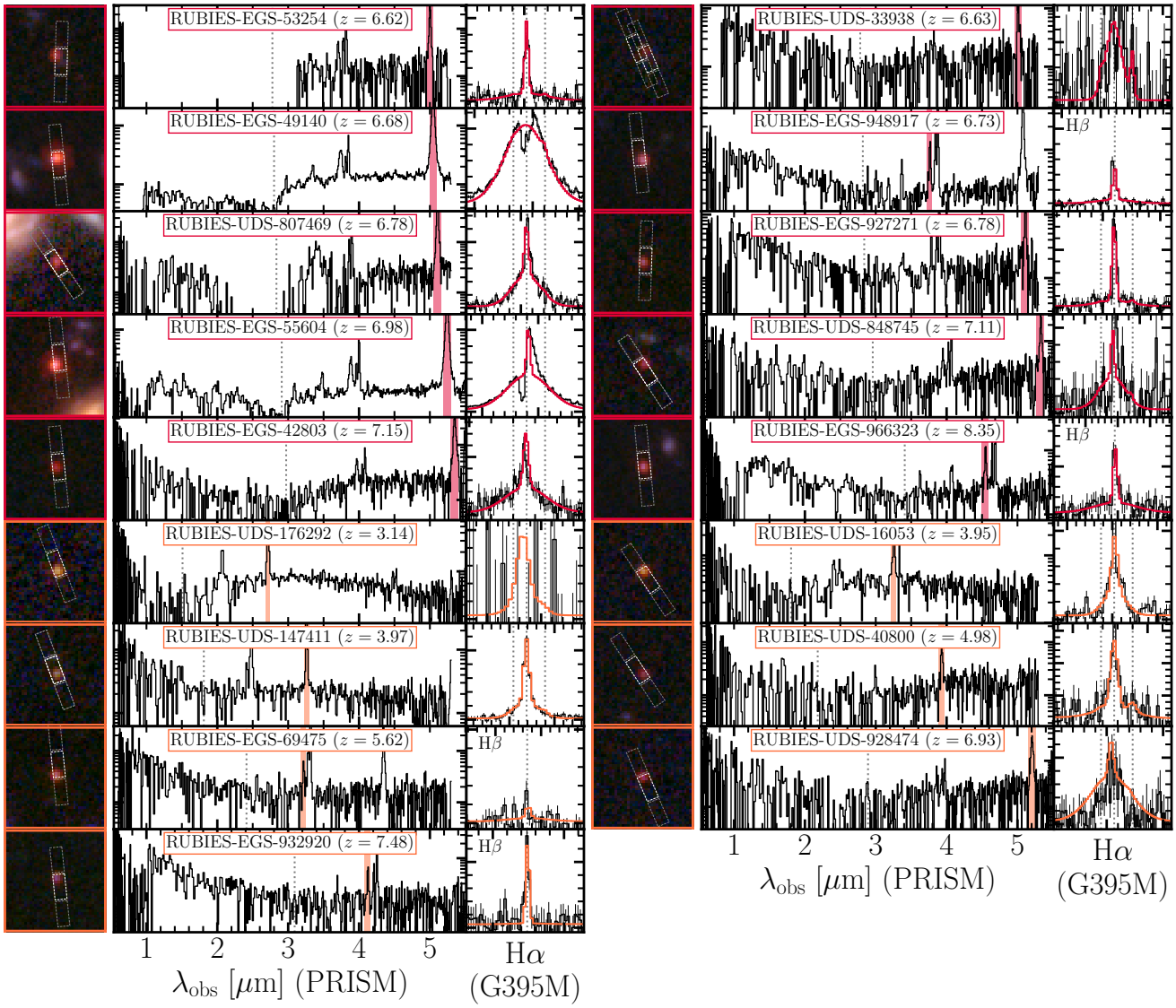


**Fig. A.2.** All RUBIES LRDs (red) found in this work followed by rest-optical point sources with v-shaped continua (orange) all organized by redshift. In each column in each row we show the following: the 1″×1″ F444W/F277W/F150W RGB cutouts (left), the log-scaled PRISM spectra with the location of the Balmer limit marked with a dashed line (middle), and the linear-scaled G395M ±3000 km s$^{-1}$ zoom-in of the H$\alpha$ line where available, otherwise H$\beta$, with the broad `unite` fit superimposed (right) (continued).

## Appendix B: Broad line sample

We present the results of our broad-line fitting, including both successful detections and cases where our fitting procedure failed due to data quality issues. In Figure B.1 we show how trace overlaps in G395M or other data quality artifacts can produce a bad fit with a broad line:

1. RUBIES-UDS-42150: Here the H$\alpha$ emission falls at the edge of the G395M spectral range, leading to data quality issues.
2. RUBIES-UDS-822719: Emission line contamination from an adjacent trace can artificially induce flux in the G395M that can be better fit with a broad component.
3. RUBIES-EGS-67278: Trace overlap may also manifest as additional continuum flux in the G395M spectrum, leading to a bad fit with a broad line.
4. RUBIES-EGS-11752: In rare cases, a line might be missing entirely from the G395M data

Our analysis identified 80 robust broad Balmer line sources and 18 potential broad-line systems The complete catalog of broad-line sources is provided in Table B.1, while Figure B.2 shows spectral zoom-ins for all robust and potential broad-line systems. However, we caution that the reported broad Balmer FWHM values are derived from Gaussian fitting with FWHM $< 2500\,\mathrm{km\,s^{-1}}$, optimized for broad line detection, that may not best represent the spectral profile.

**Table B.1.** RUBIES $z_{\rm spec} > 3.1$ broad Balmer line galaxies

| Field | ID | R.A. | Dec | $z^{\rm a}_{\rm spec}$ | ΔWAIC | Broad FWHM[b] | F444W[c] |
|---|---|---|---|---|---|---|---|
| | | J2000 | | | | km s$^{-1}$ | mag |
| UDS | 40579 | 34.244200 | −5.245871 | 3.11 | 84 | 2466 ± 31 | 21.95 |
| UDS | 143741 | 34.330086 | −5.144587 | 3.34 | 13 | 1524 ± 409 | 23.39 |
| UDS | 144195 | 34.325156 | −5.143685 | 3.36 | 143 | 2053 ± 130 | 24.52 |
| UDS | 44043 | 34.241817 | −5.239436 | 3.50 | 368 | 2371 ± 91 | 24.47 |
| UDS | 143498 | 34.417352 | −5.145051 | 3.54 | 13 | 2112 ± 343 | 23.55 |
| UDS | 154183 | 34.410749 | −5.129664 | 3.55 | 367 | 2481 ± 18 | 23.23 |
| UDS | 150323 | 34.417822 | −5.134842 | 3.62 | 74 | 1966 ± 181 | 25.21 |
| EGS | 58237 | 214.850571 | 52.866030 | 3.65 | 32 | 1976 ± 142 | 22.46 |
| UDS | 5496 | 34.405872 | −5.312951 | 3.66 | 72 | 1570 ± 208 | 24.14 |
| EGS | 15825 | 215.079264 | 52.934252 | 3.67 | 303 | 2493 ± 7 | 21.94 |
| | | | ... | | | | |

**Notes.** The full and machine-readable version of this table is available on Zenodo (Hviding et al. 2025).
[a]Based on the best DJA value.
[b]We caution that these values are derived from Gaussian fitting with FWHM $< 2500\,\mathrm{km\,s^{-1}}$ that may not best represent the spectral profile.
[c]Obtained from the Weibel et al. (2024) catalogs.

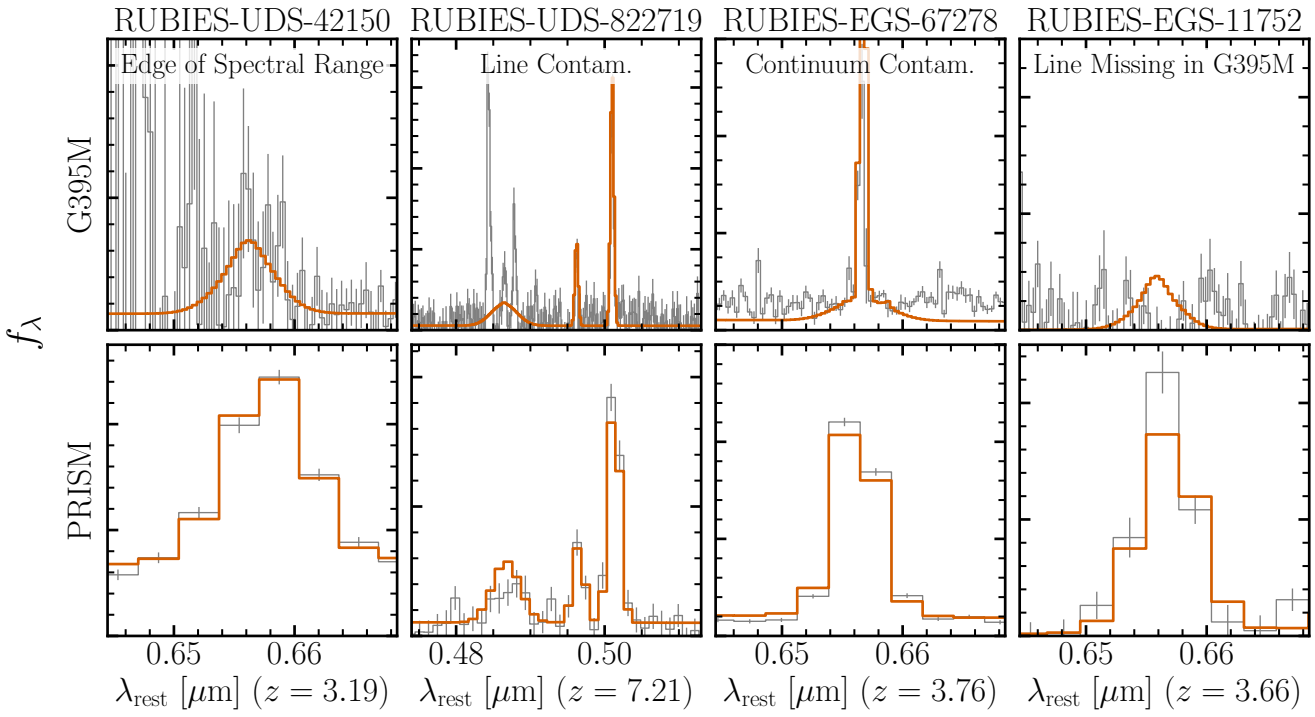


**Fig. B.1.** Examples of failed fits due to artifacts at the edge of the spectral range, emission line contamination from trace overlaps, continuum contamination from trace overlaps, and inconsistencies between G395M and PRISM extractions for RUBIES-UDS-42150, RUBIES-UDS-822719, RUBIES-EGS-67278, and RUBIES-EGS-11752 respectively.

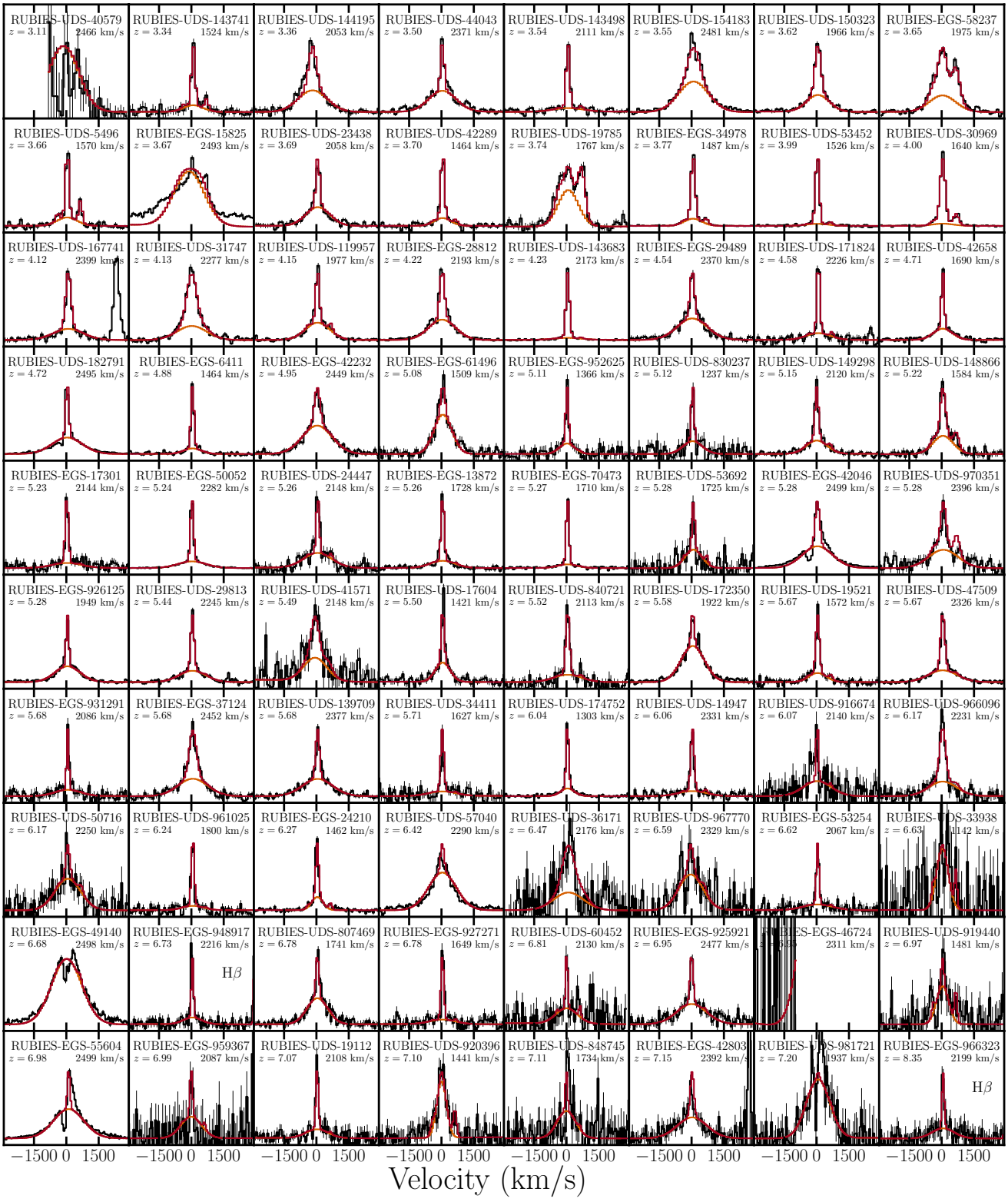


**Fig. B.2.** All robust broad Balmer line objects found in the RUBIES data, organized by redshift. We plot the linear-scaled G395M ±3000 km s$^{-1}$ zoom-in of the H$\alpha$ line where available, otherwise H$\beta$, with the broad `unite` fit superimposed in red and the broad Balmer component in orange. We also include text containing the FWHM of the broad component.